Devices for the Construction of a Cold Atom Experiment

by
Sanele Goodenough Dlamini
Submitted in fulfillment of the academic requirements for the degree of
Master of Science in
the School of Chemistry and Physics,
University of KwaZulu-Natal,
Durban,
South Africa
November 2013

Dedication

To my beautiful wife Nokuphiwa and beautiful daughter Ziphelelisiwe, thank you very much for the love and support throughout this project. If it wasn't for you, I wouldn't have made it. I love you two a lot. To my parents Mhlaselwa Dlamini and Nomusa Dlamini, thank you for encouraging me to further my studies.

Acknowledgements

Thank you to my supervisor Prof. Francesco Petruccione for giving me the opportunity to join the Quantum Research Group. Thank you for the support, motivation and supervision during all times of my research.

Thanks to Dr. Michael Morrissey for his help in the lab from the beginning of this project. Thanks for the discussions we had, they were really useful. Thanks for the guidance throughout.

I extend my thanks with sincere gratitude to my colleague Mrs Malehlohonolo Gumede (PhD student).

I would like to thank the National Research Foundation and Prof. Francesco Petruccione for funding this research.

Declaration

I confirm that this thesis is a presentation of my original research work and has not been submitted elsewhere. Where work of others has been used they have been acknowledged. The research was completed under the supervision of Prof. Francesco Petruccione at the University of KwaZulu-Natal, Durban, South Africa.

_____

Sanele Dlamini

_____

Date

_____

Prof. Francesco Petruccione

_____

Date

Abstract

The experimental setup for laser cooling and trapping of ^{87}Rb atoms with the aid of a Magneto-optical trap (MOT) is discussed. The experiment has a diverse setup, which includes: a vacuum system in which the cooling and trapping takes place; a laser system, which provides a velocity dependent force; a magnetic field,which creates a position dependent force for the atoms; and an imaging system which can be used to determine many of the properties of the atomic cloud. A polarisation detector is also designed and constructed, which is used to determine the degree of circular polarisation of beams in the experiment. Using this polarisation device, the beam can be circularly polarised to a high degree with an purity of the polarisation of 0.03. A pair of Anti-Helmholtz coils is designed and constructed, these two coils produce a magnetic field that is zero at the centre and changes linearly along along all three axes. The magnetic field gradient was measured along the symmetry axis of the coils. The final magnetic field coil measured a magnetic field gradient of 16.21 G/cm, 9.98 G/cm and 6.91 G/cm, when the separation is equal to 0.026 m, 0.655 m and 0.08 m, respectively. An overview of these systems is presented as well as their performance.

Contents

List of Figures

List of Tables

Chapter 1

Basic Theory of Laser Cooling and Trapping

1.1 Laser Cooling

Laser cooling refers to a number of techniques in which atomic and molecular samples are cooled through the interaction with one or more laser light fields [1, 2]. These techniques rely on the preferential interaction of atoms with photons which oppose their motion through the transfer of momentum during the absorption and emission of a photons. This ultimately results in the atomic sample being reduced to temperatures which are close to absolute zero in the micro-kelvin regime. Over the last two decades there has been much research of cold atoms, which has lead to many breakthroughs in numerous fields including atomic and molecular physics as well as precision metrology [3, 4, 5]. The importance of these breakthroughs has resulted in several Nobel Prizes in Physics being awarded in this field. The magneto-optical trap (MOT) has become the power-house of such experiments. Allowing researchers to routinely cool, trap and manipulate a large number of atoms at sub-Doppler temperatures for various types of experiments [6, 7].

1.1.1 Doppler Cooling

The concept of Doppler cooling provides a velocity dependant optical force by taking into account atomic velocity distributions. The force involved is the radiation pressure force, which arises from the net transfer of momentum when an atom absorbs and spontaneously emits a photon. In order to explain Doppler cooling, let us first consider an atom with a natural linewidth of Γ_A and two energy eigenstates, a ground state, a ground state $|g>$ and an excited state $|e>$ as shown in Figure 1.1. The separation between these two states is given by the atomic resonance frequency, ν_A and the coupling between the states is the Rabi frequency, which has no upper limit. The
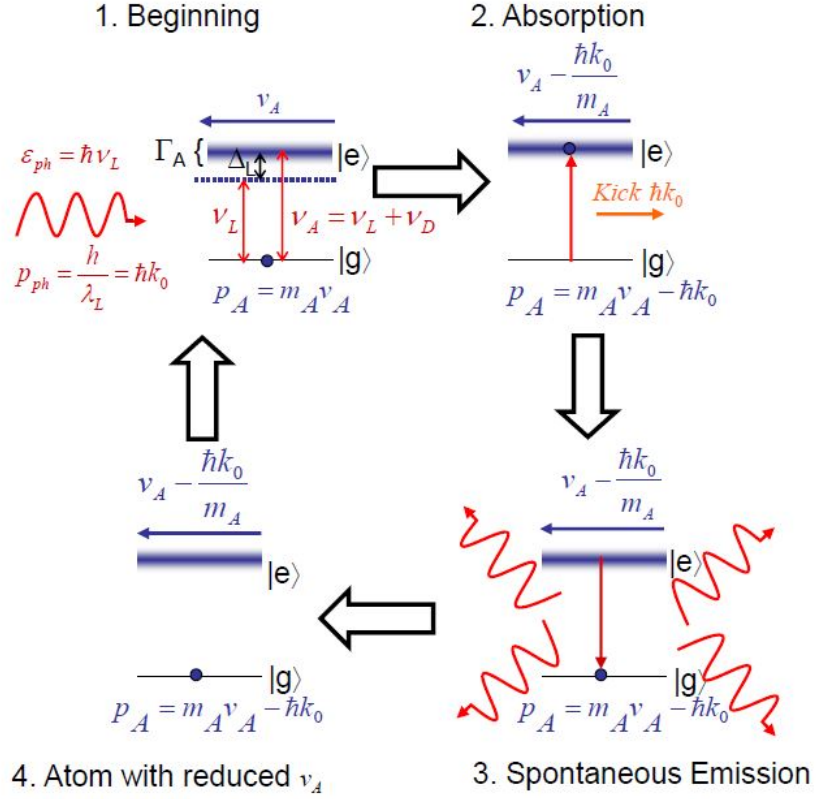
Figure 1.1: Laser Cooling Cycle

scattering rate at high intensities saturates. The saturation intensity, I_{sat} which is given by

$$I_{sat} = \frac{\pi h c \Gamma_A}{3 \lambda_A},$$ (1.1)

where h is the Planck constant, c is the speed of light, Γ_A is the natural linewidth of the excited state and λ_A is the wavelength of the transition between excited state and ground state which is given by

$$\lambda_A = \frac{c}{\nu_A}.$$ (1.2)

Consider an atom of mass m_A moving with a velocity v_A in a laser field of intensity I_L and wave vector $k_0 = \frac{2\pi}{\lambda_L}$, whose frequency is slightly detuned below the atomic resonance transition. In the above λ_L is the wavelength of the photon. From the atoms frame of reference, the laser frequency will be Doppler-shifted by an amount proportional to the velocity of the atom, $\nu_D = \pm k_0 v$. When the laser frequency is red-detuned, for atoms propagating in same direction as the laser beam the Doppler-shift is negative. Thus the

laser frequency is red-shifted away from the atomic resonance resulting in the photon not being absorbed. Atoms moving in opposite direction to the laser beam have a positive Doppler-shift and are thus blue-shifted towards atomic resonance. When the blue-shifted laser frequency is the same magnitude as the atomic resonance frequency, the atom absorbs the photon. In this case the energy of the photon is converted into internal energy resulting in the atoms being excited from the ground state to the excited state. The atom therefore experiences a momentum kick of magnitude $\hbar k_0$ in the direction of the absorbed photon and thus causes a reduction in velocity of the atom. The rate of absorption, R_{abs}, is optimum when the Doppler-shift frequency of the laser is equal to the atomic resonance. However due to the natural linewidth of the excited state, Γ_A, absorption can still occur off-resonance. The rate of absorption is therefore related to the overall detuning of the laser field and the natural linewidth of the atoms, as well the laser intensity by [1, 2, 5]

$$R_{abs} = \frac{\Gamma_A}{2} \frac{I_L}{I_{sat}} \left[\frac{1}{1 + \left[\frac{2(\Delta_L + \nu_D)}{\Gamma_A} \right]^2} \right], \tag{1.3}$$

where $\Delta_L = \nu_L - \nu_A$ is the detuning of the laser frequency from the atom's resonance transition in the reference frame of the laboratory. Provided the laser intensity is low compared to the saturation intensity of the atom, after the lifetime of the excited state, the atoms spontaneously decay to the ground state emitting photons in random directions. This causes the atom to recoil in the opposite direction to the emitted photon. The scattering rate R_{scat}, due to spontaneous emission is given by [1, 2, 5]

$$R_{scat} = \frac{\Gamma_A}{2} \frac{I_L}{I_{sat}} \left[\frac{1}{1 + \frac{I_L}{I_{sat}} + \left[\frac{2(\Delta_L + \nu_D)}{\Gamma_A} \right]^2} \right]. \tag{1.4}$$

During spontaneous emission the atom experiences a random momentum kick $\hbar k_0$ in the opposite direction to the spontaneously emitted photon. Over a course of many absorption and emission cycles, the net momentum change due to spontaneous emission is zero due to the average symmetry of the spontaneous emissions. Thus the only force acting on the atom on average is the radiation pressure force caused by the absorption process. This reduces the velocity of the atom with each cycle, as shown on Figure 1.1 where the atom follows these steps $1 \rightarrow 2 \rightarrow 3 \rightarrow 4 \rightarrow 1$. Over N cycles the velocity is reduced by $\frac{N\hbar k}{m_A}$.

The radiation pressure force, F_{rp}, always acts to accelerate the atom in the direction of propagation of the laser field, this meas that it opposes the motion of the atom and is given by

$$F_{rp} = \pm \frac{\hbar k_0 \Gamma_A}{2} \frac{I_L}{I_{sat}} \left[\frac{1}{1 + \frac{I_L}{I_{sat}} + \left[\frac{2(\Delta_L + \nu_D)}{\Gamma_A} \right]^2} \right]. \tag{1.5}$$

This force saturates at $\frac{\hbar k_0 \Gamma_A}{2}$ for large intensities when $I_L > I_{sat}$ due to the increased stimulated emission rate. In the case where the stimulated emission rate becomes dominant over spontaneous emission, cooling only occurs for blue detuning. This cooling is stronger than the Doppler cooling, but does not achieve as low a temperature. Doppler cooling, therefore, only occurs for light intensities below the saturation intensity when $I_L < I_{sat}$ and the rate of spontaneous emission is dominant over stimulated emission.

1.1.2 Optical Molasses

The previous section considered the case of an atom interacting with a single laser field. Optical molasses (OM) is formed when atoms are allowed to interact with two counter-propagating laser fields, which are identical in intensity and the frequency of which is slightly red detuned relative to the atomic resonance as shown in Figure 1.2(a). Here one assumes that the light intensity is less than the saturation intensity, so that stimulated emission can be ignored or neglected. The Doppler effect causes the atom to observe the laser fields at different frequencies depending on whether it is co- propagating or counter-propagating with respect to the laser beam direction. In the atoms frame of reference the co-propagating beam is red shifted away from resonance ($\nu'_L = \nu_L - k_0 v_A$), but the atom sees the counter-propagating beam blue shifted toward resonance ($\nu'_L = \nu_L + k_0 v_A$) as shown in Figure 1.2(b). Therefore, the atoms will preferentially absorb photons from the counter propataing beam which opposes its motion and gives rise to a viscous damping force. This is called 1-D optical molasses. The average force on the atom in optical molasses F_{OM} is the sum of the forces of the the two individual beams given by [1, 5]:

$$F_{OM} = \pm \frac{\hbar k \Gamma}{2} \frac{I_L}{I_{sat}} [\frac{1}{1 + \frac{I_L}{I_{sat}} + (\frac{2(\Delta_L \mp k_0 v_A)}{\Gamma_A})^2}]. \quad (1.6)$$

When the velocity approaches zero, F_{OM} varies linearly with velocity. Here the total force can be written as

$$F_{OM} = \alpha_{OM} v_A, \quad (1.7)$$

where α_{OM} is the optical molasses frictional coefficient. For a negative detuning this force damps the atomic motion with the positive friction coefficient. The force is therefore slowing down the atoms. The optical molasses coefficient is given by [1, 5]

$$\alpha_{OM} = -4\hbar k_0 \frac{I_L}{I_{sat}} [\frac{\frac{2\Delta_L}{\Gamma_A}}{1 + \frac{2I_L}{I_{sat}} + (\frac{2\Delta_L}{\Gamma_A})}]. \quad (1.8)$$

When the laser intensity is low and the detuning is small, α_{OM} varies linearly with both the parameters. For larger values of each parameter α_{OM}

(a) Laboratory Frame

v_A

$|e\rangle$

Δ_L

$v_L = v_A - \Delta_L$

$v_L = v_A - \Delta_L$

v_L v_A

$|g\rangle$

(b) Atomic Frame

v_A

$|e\rangle$

Δ_L

$\vec{v}'_L = v_L + k v_A$

$\overleftarrow{v}'_L = v_L - k v_A$

$\vec{v}'_L$ $\overleftarrow{v}'_L$

$|g\rangle$

Doppler blue shifted, F_{rp+}

Doppler red shifted, F_{rp-}
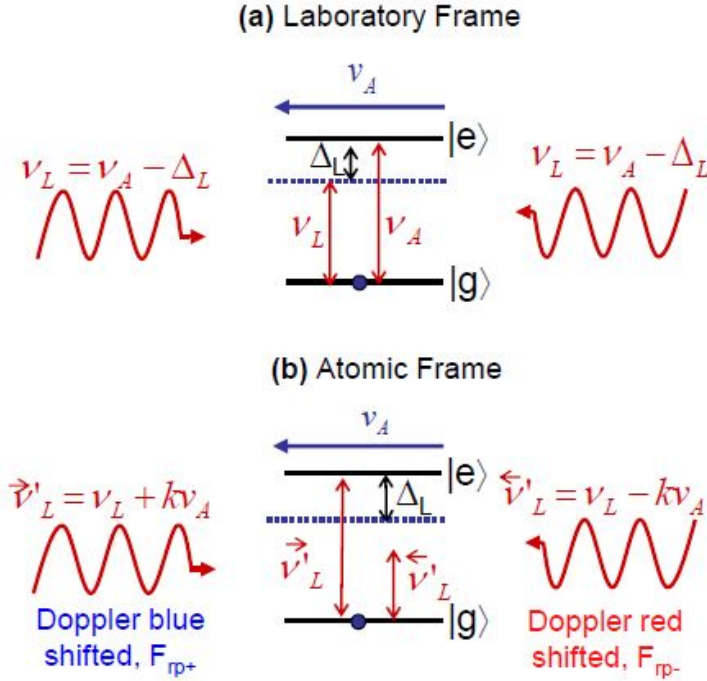
Figure 1.2: Optical molasses (a) taken in the laboratory frame of reference; (b) taken in the atomic frame of reference

saturates at $\frac{\hbar k_0^2}{4}$ when $\frac{I_L}{I_{sat}} = 2$ and $\Delta_L = \frac{-\Gamma_A}{2}$ and then decreses. By using three pairs of counter propagating orthogonal beams all intersecting at a point it is possible to slow the atoms in all three dimensions creating a 3-D optical molasses.

The heating effect caused by spontaneous emission balances with the cooling effect producing the Doppler cooling limit, T_D given by [8]

$$T_D = \frac{\hbar \Gamma_A}{2 k_B},\tag{1.9}$$

where k_B is the Boltzmann constant. The Doppler limit of ^{87}Rb calculated using equation 1.9 is $\sim 150\ \mu$K. Though the atoms are cooled, they are free to move around the laser intersection region due to the absence of a position dependant force that would bring them back to a single equilibrium position. Atoms can easily escape the cooling region due to inter-particle collisions and continuous absorption and emission of photons.

5
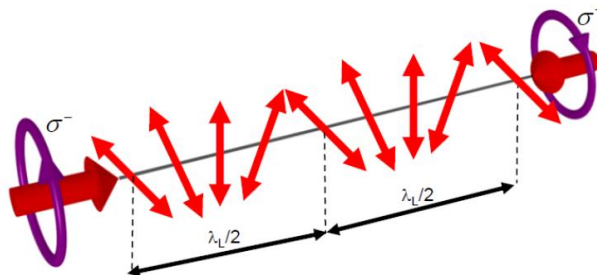
Figure 1.3: Resultant polarisation gradient from two oppositely circularly polarised counter-propagating laser beams.

1.1.3 Sub-Doppler Cooling

In the 1980's as experimentation into laser cooling progressively continued, different configurations of beam polarisations and detunings were tested [9]. The techniques for temperature measurement were also being developed. During this time temperatures that were below the Doppler limit were also observed. From these findings it was clear that new theories needed to be developed, that will take more than considering just intensity and detuning of the beams. We only concentrate on $\sigma^+ - \sigma-$ polarisation gradient cooling as it is what takes place in a MOT in our experimental setup. In $\sigma^+ - \sigma^-$ polarisation gradient cooling, the gradient is made up of two counter-propagating laser beams with intensities which are equal, and with orthogonal circular polarisation. The beam frequencies are the same and are slightly red-detuned from the atomic resonance frequency, as shown on Figure 1.3.

Let us consider an atom with a ground state $J_g = 1$ and an excited state $J_e = 2$, as shown in Figure 1.4. When the atom is at rest optical pumping redistributes the population among the magnetic sub-states according to the local direction of the polarization vector. The ground state level $m_g = 0$ is populated the most compared to the $m_g = \pm 1$ sublevels. This is due to that the fact that rate of optical pumping from $m_g = -1$ to $m_g = 0$ is greater than the optical pumping rate from $m_g = 0$ to $m_g = -1$. Atoms which are moving encounter a rotation of the quantisation axis and must be optically pumped in order to follow it. The difference in scattering rates results in a radiation force, that opposes the motion of the atoms. Causing the atoms to be cooled below the the Doppler limit. This technique also has a cooling limit determined by the energy the atom gains through spontaneous emission. The recoil limit for ^{87}Rb is given by: [10]

$$T_R = \frac{(\hbar k_0)^2}{m_A k_B}. \tag{1.10}$$

The recoil limit of ^{87}Rb is about 361.96 nK. Cooling beyond this limit is
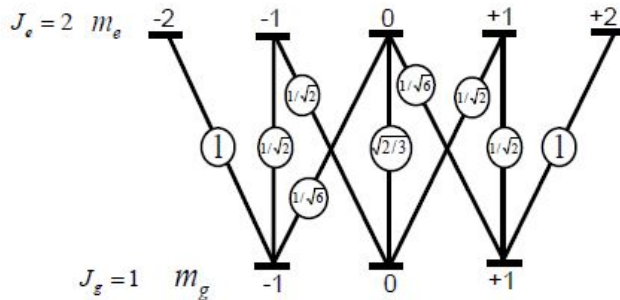
Figure 1.4: Clebsch-Gordon coefficients for a $J_g = 1 \to J_e = 2$ system.

possible and has taken place, in Raman cooling, velocity selective coherence population trapping and evaporative cooling. These advanced cooling methods have allowed the achievement of Bose-Einstein condensates.

1.1.4 Magneto Optical Trap

The Magneto-optical trap (MOT) consist of anti-Helmholtz coils to provide a spatially dependent force and laser beams which provide a velocity dependent force. A pair of coils are said to be in anti-Helmholtz configuration when they are placed symmetrically along their axis, with each coil carrying a current equal in magnitude but opposite in direction. Anti-Helmholtz coils provide a spherical quadrupole magnetic field which, in combination with the light fields, forces the atoms to the center of the coils. The shift in the energy levels affects the rate at which atoms at various positions scatter photons from the laser beams. The trapping force can be best described and explained using an atomic two level system, where $J_g = 0$ represents the ground state and $J_e = 1$ represents the excited state as illustrated in Figure 1.5(a). Due to the presence of the magnetic field, the magnetic sublevels are no longer degenerate and thus have have a separation defined by the magnitude and direction of the magnetic field. This is known as Zeeman splitting and in combination with the varying magnetic field, the separation of the magnetic sublevels is thus dependent on the position in space. This can be seen in figure 1.5(b) where the relative separation of the levels $m_e = 0, +1, -1$ are depicted for different positions. Due to the selection rule the σ^- polarised light only causes a transition at which the change in magnetic spin quantum number by $\Delta m = -1$, and the σ^+ polarised light only causes a transition in which the change by $\Delta m = +1$. Consider an atom navigating at an almost zero velocity at the position where $Z > 0$ and $B > 0$ on Figure 1.5(b). The atom will encounter a Zeeman splitting such that the $m_e = -1$ transition is tuned closer to resonance and the scattering rate of the σ^- photons increases. The $m_e = +1$ transition is tuned further
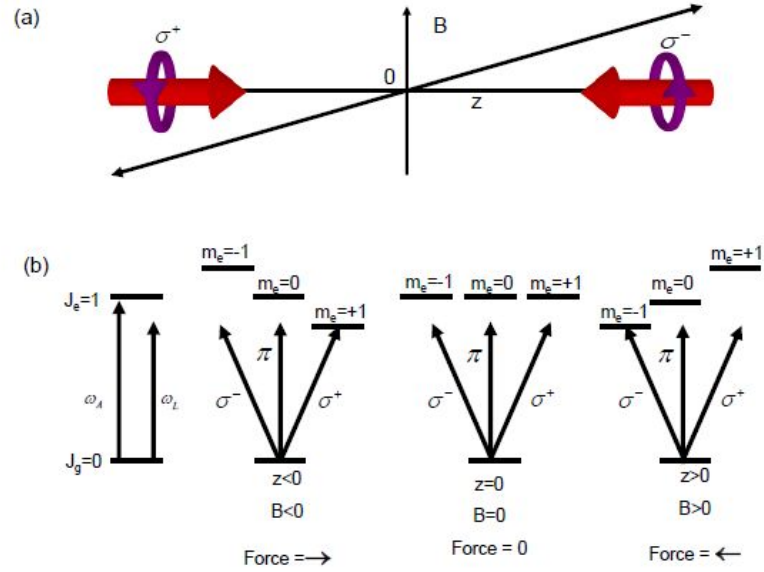
Figure 1.5: a) MOT setup showing linear magnetic field and two cicular polirised beams moving in opposite direction. (b) the variation of the Zeeman splitting and the coupling of these transition to the ground state as a function of position.

away from resonance and will decrease the scattering rate of the σ^+ photons. Thus the atoms interact with the counter propagating σ^- laser field and that results in a net force in the direction of propagation of the σ^- beam. This pushes the atom towards the centre of the trap. When an atom is moving at a position where $Z < 0$ and $B < 0$ the $m_e = +1$ transition is tuned closer to resonance with the σ^+ laser beam and the atom is forced to the centre of the trap. This concept can be extended to 3-D whereby atoms are cooled and trapped in all three spacial dimensions resulting in a cloud of cold atoms at the centre. Figure 1.6 shows a 3-D schematic of the MOT, with a quadrupole magnetic field produced by anti-Helmoltz coils, and three pairs of red-detuned counter-propagating laser beams.

1.1.5 Atomic Structure

Cesium (Cs), sodium (Na) and rubidium (Rb) are some of the atomic elements that may be used for the purpose of laser cooling and trapping of atoms. In our experiment we use ^{87}Rb. This is a soft silvery metal and it is an active chemical element. It is a member of the alkali Group I family in the periodic table. ^{87}Rb has 37 electrons of which one is a valance electron. The ^{87}Rb atom has two D line transitions named D$_1$ ($5^2S_{\frac{1}{2}} \rightarrow 5^2P_{\frac{1}{2}}$) at 795
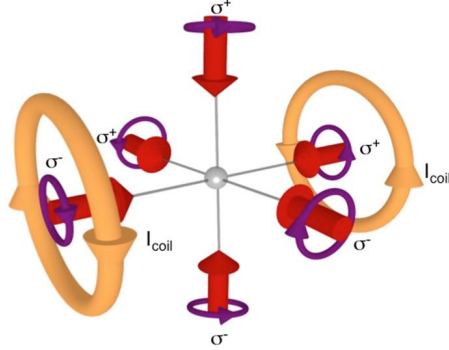
Figure 1.6: Schematic description of 3-D cooling [5].

nm and D_2 ($5^2S_{\frac{1}{2}} \to 5^2P_{\frac{3}{2}}$) at 780 nm. The latter transition is the one that is of importance to us, as it has the cycling transition that we use for laser cooling [11].

An atom is made up of protons, neutrons and electrons, which have a spin. The nucleons give the atom its nuclear spin $\mathbf{I}$ which is I=3/2 for Rb. The total angular momentum of the electron is given by

$$\mathbf{J} = \mathbf{S} + \mathbf{L}, \tag{1.11}$$

where $\mathbf{S}$ is the spin of the electron and $\mathbf{L}$ is the orbital angular momentum of electron, in the ground state, L=0 and J=1/2. Total atomic angular momentum is given by

$$\mathbf{F} = \mathbf{I} + \mathbf{J}, \tag{1.12}$$

where $\mathbf{J}$ is the total electronic angular momentum. The coupling produces the hyperfine structure of the atom. The ground states of the ^{87}Rb atom are F_g=1 and F_g=2 and are separated by 6.83 GHz. 2F+1 degenerate magnetic sublevels exist for each hyperfine level. In a magnetic field $\hat{\mathbf{B}}$ the degeneracy is activated. The interaction between the atoms and $\hat{\mathbf{B}}$ is given by

$$H_B = \frac{\mu_B}{\hbar}(g_S\mathbf{B} + g_L\mathbf{L} + g_I\mathbf{I}) \cdot \mathbf{B}. \tag{1.13}$$

In the above equation μ_B is the Bohr magneton and g_S, g_L, g_I are the gyromagnetic ratios. When we have a weak magnetic field and a small shift, the interaction between the atoms and magnetic field is reduces to

$$H_B = \mu_B g_F F_z B_z, \tag{1.14}$$

here the magnetic field is along the z-axis. This produces an energy shift of

$$\Delta E = g_F m_F \mu_B B_z, \tag{1.15}$$

where g_F is the Landé g-factor and m_F is the magnetic quantum number. The shift in the energy is called the Zeeman effect.

The cooling and trapping of atoms is done by one laser, slightly red-detuned from $(5^2S_{\frac{1}{2}}), F_g = 2 \rightarrow (5^2P_{\frac{3}{2}}), F_e = 3$ state, as shown on Figure 1.7. The laser is locked using standard saturation absorption spectroscopy (SAS) technique. About one in every thousand atoms excited to F_e=3 state will decay to F_g=1 state. This results in the atom being out of resonance with the cooling laser and thus are no longer cooled or trapped. To prevent this we need another laser operating which excites atoms from F_g=1 to F_e=2 state where they can decay back to the F_g=2 and are thus able to interact with the trapping laser beams. The second laser is known as the pumping laser. Table 1.1 gives a summary of atomic properties for ^{87}Rb that are important when referring to laser cooling and trapping experiments.
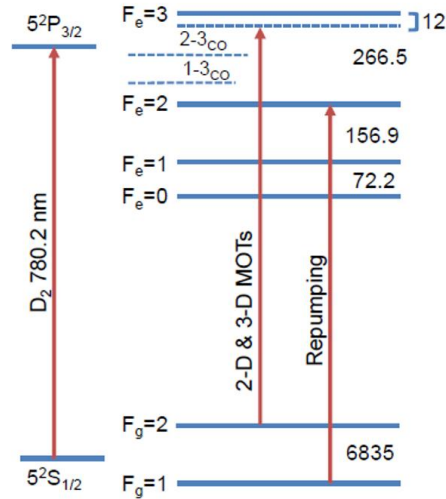
Figure 1.7: Hyperfine structure of ^{87}Rb.

Table 1.1: Properties of ^{87}Rb.

Parameter	Symbol	Value
Mass	m	87 amu
Nuclear Spin	I	3/2
D_2 Transition Wavelength	λ_A	780.25 nm
Lifetime	τ	26.2 ns
Decay Rate	Γ_A	2π·6.07 MHz
Recoil Velocity	v_r	6 mm/s
Saturation intensity	I_{sat}	3.58 mW/cm^2
Recoil Temperature	T_r	361.96 nK

Chapter 2

Creation of a Ultra High Vacuum System

2.1 Construction and Design

A schematic diagram of the vacuum system is shown in Figure 2.1(a). The setup consists of an ion pump, a titanium sublimation pump, a pumping valve to allow initial pumping of the vacuum system and a MOT chamber. The MOT chamber is a stainless steel octogonal chamber which has seven DN40 ports around the octogonal surface and two DN100 viewports at the front of and back of the face. These viewports allow optical access of the cooling beams and imaging systems. The vacuum system contains a rubidium ampule which continuously releases a rubidium vapour due to out gassing. The ultra high vacuum (UHV) pressure is maintained with the aid a a titanium sublimation pump and an ion pump (150 l/s). When the system was put together, copper gaskets were used when connecting all of the flanges which allow UHV parameters to be achieved. All the components were cleaned with acetone before they were connected. The MOT chamber and the ion pump are supported by aluminium stands, which are clamped on the optical table.

2.1.1 High Vacuum

To create a vacuum four pumps were used, the scroll pump, a turbo-molecular pump (TMP), an ion pump and the titanium-sublimation pump. All these pumps work at different ranges of pressure as shown in Figure 2.1. At this stage the vacuum system has been cleaned using acetone to get rid of large contaminants. A combined TMP and scroll pump is attached to the pumping port and the pumps are switched on. Initially the scroll pump pumps the entire system down to 2×10^{-2} mbar. At this point the TMP switches on automatically and begins pumping in conjunction with the scroll pump.
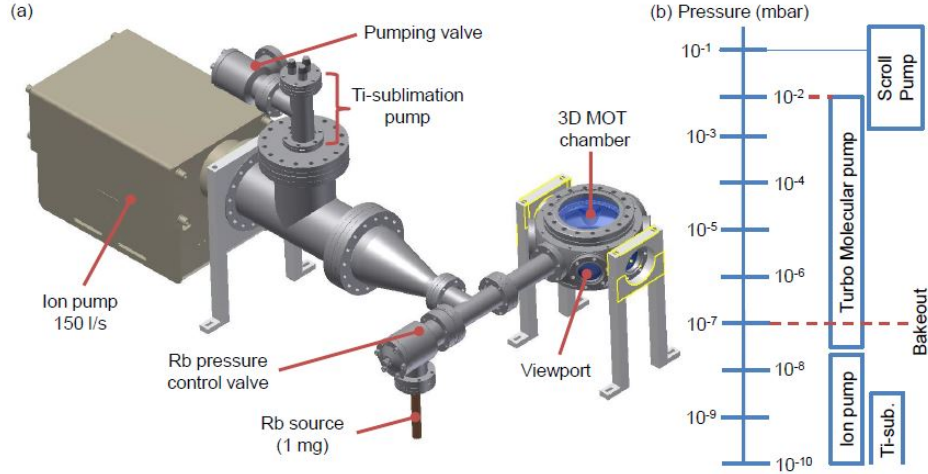
Figure 2.1: a) Diagram showing the vacuum setup and b) pumping techniques and pressure readings.

A pressure of 10^{-7}mbar was achieved in a few hours when using the above mentioned pumps.

2.1.2 Ultra High Vacuum

To achieve a good MOT, ultra high vacuum (UHV) conditions are required. Atoms desorb from the inner vacuum wall and MOT chamber wall, destroying the vacuum. This process is called outgassing. Baking the vacuum system forces the atoms absorbed on and dissolved from the inner walls of the vacuum system, so that the process of outgassing does not destroy the vacuum. [12, 13, 14]

The vacuum system is wrapped evenly with electrical heating tapes and covered with aluminum foil. The foil is used as a thermal insulator, this allows even heating of the system. Thermocouples are then placed at different locations of the vacuum system underneath the foil layers to monitor the temperature. Six power supplies supply current to the heating tapes. The temperature is increased at a low rate until it reaches a temperature of 300^0C. Increasing the vacuum temperature at a higher rate would lead to the exposure to irreversible thermal stress of the vacuum components. The system is then baked out for a period of two days at 300^0C. The TPM has to be operational during bake out The system is then cooled down and the vacuum is sealed.The ion pump and the titanium sublimation pump will only work work on a pressure that is already as low as about 10^{-7}mbar after bake out. The pressure is maintained using an ion pump and a base pressure

of 2×10^{-10} mbar which is sufficient for our experimental purposes.

2.1.3 Atom Source

When we achieve the UHV, a background vapour of rubidium needs to be created inside the vacuum chamber. The atom source is introduced into the vacuum system with the aid of a 1 mg rubidium ampule, whose pressure is controlled by a Rb pressure control valve. The ampule is located inside the copper tube. If this does not work, one can pass an electric current through to the source. To test for the presence of background vapour of rubidium in the chamber, a laser which is tuned to the transition of ^{87}Rb is passed through the vacuum chamber. This process is done until fluorescence is seen with the aid of a CCD camera.

Chapter 3

Optical Devices

3.1 Testing Polarisation Components

When one uses a MOT to create cold atoms, the cooling is done by circular polarised beams. It is very important and useful to have a simple hand held device, which will detect the degree of circular polarisation of the beam. This device will be made of several polarisation optics such as polarising beam splitters, polarisers and waveplates. It is thus necessary to become familiar with the operation of optics.

3.1.1 Half-wave plate and PBS

The polarising beam splitter (PBS) is an optical device that splits light into two different polarisation components and the half-wave plate shifts the polarisation direction of linearly polarised light. Consider the setup as shown in Figure 3.1(a). The beam passes through the half-wave plate which will be rotated, then to the polarising beam splitter where it is split into two beams. The power of these beams is measured by the photodiode. The half-wave plate was rotated in increments of 10^0 and the power of each beam was recorded. The results can be seen on Figure 3.1(b), where reflected and transmitted powers are normalised. It can be clearly seen that the powers go from maximum to minimum over a period of 45^0 of half-wave plate physical rotation. By rotating the half-waveplate ($\frac{\lambda}{2}$) by 45^0 we rotate polarisation by 90^0. This implies that the light beam goes from vertical to horizontal in 45^0 ratation of the half-wave plate. This allows us to have a linear polarisation which are orthogonal to each other with a high degree of polarisability in each leg of of the PBS. The half-waveplate also affords us the ability to control power outputs at PD1 and PD2 and to have a high degree of polarisability on each PBS leg .

When light propagates through the half-waveplate and PBS, it undergoes changes in its polarisation. Using the Jones matrix the polarisation of light

can be explained mathematically. The light is linearly polarised at 45^0 from the horizontal x-axis, when it leaves the optical isolator. The z-axis is the direction light propagates. The Jones matrix is given by [15]

$$\frac{1}{\sqrt{2}} \begin{bmatrix} 1 \\ 1 \end{bmatrix}. \tag{3.1}$$

The light then goes through a half-wave plate which has the Jones matrix given by

$$\begin{bmatrix} \cos 2\theta & \sin 2\theta \\ \sin 2\theta & -\cos 2\theta \end{bmatrix}, \tag{3.2}$$

where θ is the angle made by the fast axis with respect to the horizontal x-axis. The angle can be adjusted so that one can control the ratio of horizontal and vertical polarised light. If one were to set θ to 15^0 then the resultant linear polarisation would be given by

$$\frac{1}{\sqrt{2}} \begin{bmatrix} \cos 2\theta & \sin 2\theta \\ \sin 2\theta & -\cos 2\theta \end{bmatrix} \begin{bmatrix} 1 \\ 1 \end{bmatrix} = \begin{bmatrix} 0.97 \\ -0.26 \end{bmatrix}. \tag{3.3}$$

More light would have polarisation along the horizontal x-axis than along the vertical y-axis. When the light enters the PBS, the horizontally and vertically polarised light is separated into two beams, the respective intensities of the beams depends on the orientation of the half-waveplate. The Jones Matrix for PBS is given by

$$\frac{1}{2} \begin{bmatrix} 1 & 1 \\ 1 & 1 \end{bmatrix}. \tag{3.4}$$

Therefore in Figure3.1(a) the analytical expression for the photodiode is given by

$$\frac{1}{2\sqrt{2}} \begin{bmatrix} 1 & 1 \\ 1 & 1 \end{bmatrix} \begin{bmatrix} \cos 2\theta & \sin 2\theta \\ \sin 2\theta & -\cos 2\theta \end{bmatrix} \begin{bmatrix} 1 \\ 1 \end{bmatrix} \tag{3.5}$$

and it simplifies to

$$\frac{1}{2\sqrt{2}} \begin{bmatrix} 2\sin 2\theta \\ 2\sin 2\theta \end{bmatrix}. \tag{3.6}$$

This analytical expression of the photodiode applies to only one of the two outputs of the PBS.

3.1.2 Polariser

A polariser allows light of a certain polarisation to pass through and blocks waves of other polarisations. When using a polariser it is useful to know its optical axis. We therefore need to determine the the optical axis of the polariser. To do this we follow the setup as shown in Figure 3.2(a). The
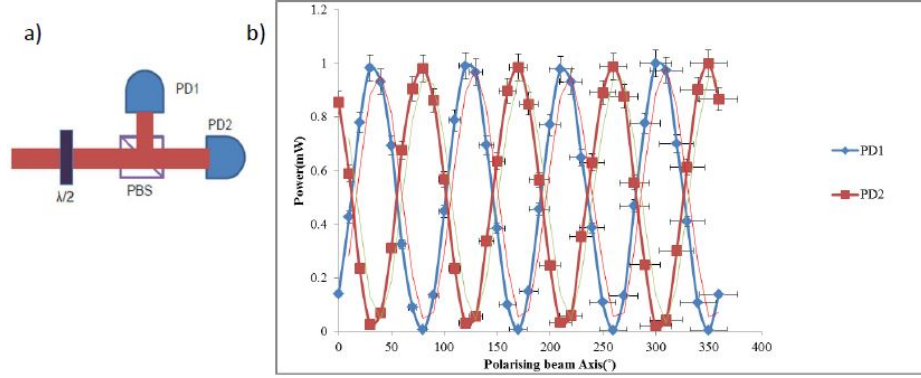
Figure 3.1: a) Control of power output of PD1 and PD2 and b) Angles to control power. The red curve is theoretical fit for PD1 and the green curve is theoretical fit for PD2.

combination of the half-wave plate and the PBS creates a highly linear polarisation to act as a test beam for the polariser. The light beam passes through the, half-wave plate and the PBS providing us with a single polarisation and the ability to control its power. The beam then passes through the polariser under test and the power is then measured on a photodiode(PD). Figure 3.2(b) shows the maximum and minimum values for rotating of polariser. For maximum values the polariser is parallel with polarisation of light and for minimum values the polariser is perpendicular to polarisation of light. The maximum values are $256^0, 74^0$ and the minimum are $156^0, 336^0$. Therefore every 90^0 the polariser is either parallel or perpendicular with light. This gives us the ability to allow certain polarisation through and block other polarisation.

The polariser has a Jones matrix given by

$$\begin{bmatrix} \cos^2\theta & \sin\theta\cos\theta \\ \sin\theta\cos\theta & \sin^2\theta \end{bmatrix}. \tag{3.7}$$

In Figure 3.2(a)the analytical expression of the photodiode is given by

$$\frac{1}{2\sqrt{2}} \begin{bmatrix} \cos^2\theta & \sin\theta\cos\theta \\ \sin\theta\cos\theta & \sin^2\theta \end{bmatrix} \begin{bmatrix} 1 & 1 \\ 1 & 1 \end{bmatrix} \begin{bmatrix} \cos 2\theta & \sin 2\theta \\ \sin 2\theta & -\cos 2\theta \end{bmatrix} \begin{bmatrix} 1 \\ 1 \end{bmatrix}, \tag{3.8}$$

which simplifies to

$$\frac{1}{\sqrt{2}} \begin{bmatrix} (\cos^2\theta + \cos\theta\sin\theta)\sin 2\theta \\ (\sin^2\theta + \cos\theta\sin\theta)\sin 2\theta \end{bmatrix}. \tag{3.9}$$

16
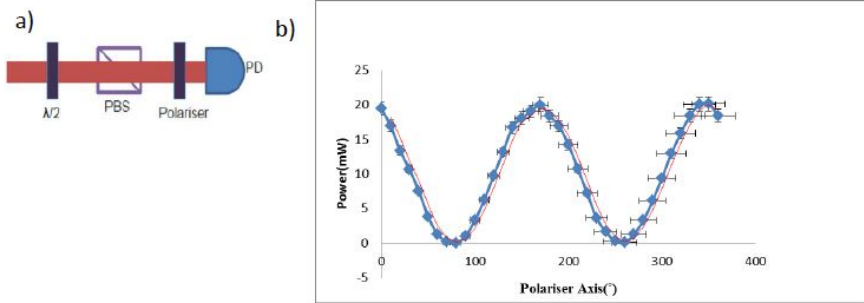
Figure 3.2: (a) Schematic setup for determining the optical axis and (b) optical access of polariser. The red curve is a theoretical fit.)

3.1.3 Optical Axis of Half-wave plate

By adopting the above setup in Figure 3.2, the optical axis of the half-wave plate can also be determined. The following setup as shown in Figure 3.3(a) was set up. The beam passes through the $\frac{\lambda}{2}$, to the PBS, to the waveplate ($\frac{\lambda}{2}$(a)) which is tested (rotated), then to the polariser which is set at 256^0 maximum optical axis of polariser and to the photodiode. Figure 3.3(b) shows maximum and minimum values. For maximum values the optical access of light passes through half-wave plate unaffected and for minimum values $\frac{\lambda}{2}$(a) has rotated polarisation by 90^0, thus it is perpendicular to polariser and gets blocked.

The analytical expression of the photodiode intensity in Figure 3.3(a) using Jones matrices is given by

$$\frac{1}{2\sqrt{2}} \begin{bmatrix} \cos^2\theta & \sin\theta\cos\theta \\ \sin\theta\cos\theta & \sin^2\theta \end{bmatrix} \begin{bmatrix} \cos 2\theta & \sin 2\theta \\ \sin 2\theta & -\cos 2\theta \end{bmatrix} \begin{bmatrix} 1 & 1 \\ 1 & 1 \end{bmatrix} \times$$

$$\begin{bmatrix} \cos 2\theta & \sin 2\theta \\ \sin 2\theta & -\cos 2\theta \end{bmatrix} \begin{bmatrix} 1 \\ 1 \end{bmatrix} = \frac{2}{\sqrt{2}} \begin{bmatrix} \cos^2\theta\sin\theta(\cos\theta+\sin\theta) \\ \cos\theta\sin^2\theta(\cos\theta+\sin\theta) \end{bmatrix}. \quad (3.10)$$

3.1.4 Optical Axis of Quarter-wave plate

The quarter-wave plate is an optical device that which converts linearly polarised light into circular polarised light and it also converts circular polarised light to linearly polarised light. The optical axis of the quarter-wave plate is also determined, see Figure 3.4(a) for setup. By setting the polariser to maximum optical axis, as we rotate the quarter-wave plate the

17
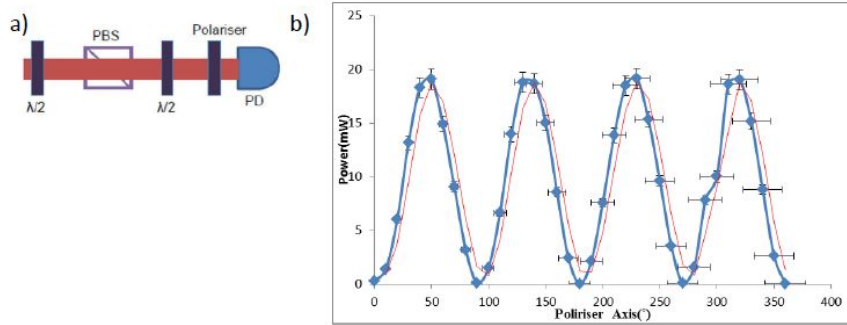
Figure 3.3: (a) Schematic setup of a half-waveplate ($\frac{\lambda}{2}$) function and (b) optical axis of half-wave plate.The red curve is a theoretical fit.)

power goes from maximum to half of the maximum. We need to create a beam with circular polarisation to test the detector, see setup on Figure 3.4. The input beam passes through a half-wave plate whose orientation will determine how much power is transmitted through a polarising beam splitter (PBS) which follows. The beam then passes through a quarter-wave plate which rotates beams polarisation. The amount of rotation depends on the relative angle between the optical axis of the quarter-waveplate and the beam itself. The quarter-waveplate can be used to create σ^+/σ^- polarised light from linearly polarised light at a specific orientation. The beam is then retro-reflected back on itself using a dielectric mirror which maintains the polarisation on reflection. After passing through the quarter-wave plate for the second time the beam's polarisation is again rotated by an amount proportional to the angle between the optical axis of the quarter-wave plate and the beam. The amount of power being transmitted or reflected through the beam splitter depends on the orientation of the quarter-waveplate. The reflected light on the second pass is measured using a power meter. When there is a maximum or minimum measured at this particular point we know that we either have σ^+ or σ^- circular polarised light. These are the quarter-waveplate degree angles for which σ^+/σ^- were observed. The maximum are $40^0, 130^0, 222^0, 312^0$ and the minimum are $88^0, 176^0, 266^0, 356^0$ as shown in Figure 3.4(b).

The Jones matrix for the quarter-waveplate is given by

$$\mathbf{e}^{i\frac{\pi}{4}} \begin{bmatrix} 1 & 0 \\ 0 & i \end{bmatrix} \tag{3.11}$$

and the Jones matrix for the mirror is given by

$$\begin{bmatrix} 1 & 0 \\ 0 & -1 \end{bmatrix}. \tag{3.12}$$

18

The analytical expression for the photodiode intensity in Figure 3.4(a) is given by

$$\frac{\mathbf{e}^{i\frac{\pi}{4}}}{2\sqrt{2}} \begin{bmatrix} 1 & 0 \\ 0 & -1 \end{bmatrix} \begin{bmatrix} 1 & 0 \\ 0 & i \end{bmatrix} \begin{bmatrix} 1 & 1 \\ 1 & 1 \end{bmatrix} \times$$

$$\begin{bmatrix} \cos 2\theta & \sin 2\theta \\ \sin 2\theta & -\cos 2\theta \end{bmatrix} \begin{bmatrix} 1 \\ 1 \end{bmatrix} = \frac{-1}{\sqrt{2}} \begin{bmatrix} \sin 2\theta \\ i \sin 2\theta \end{bmatrix}. \tag{3.13}$$
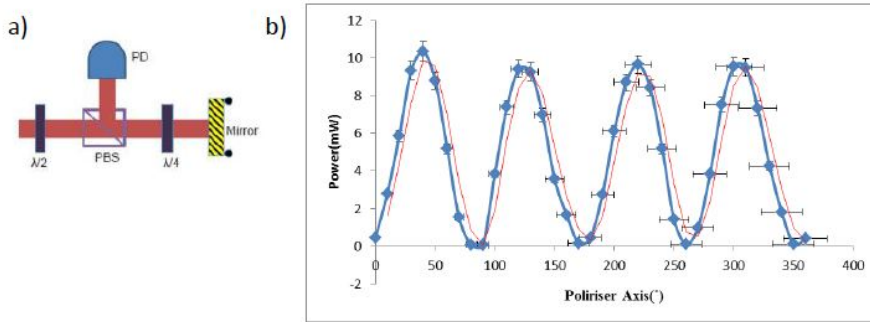
Figure 3.4: a) Schematic setup to create a beam with circular polarisation. b) A plot of power against optical axis showing maximum and minimum values when rotating the quarter-wave plate.The red curve is a theoretical fit.)

3.1.5   Test for Circular Polarised Light

Using the above technique we now have σ^+/σ^- light. In Figure 3.4 the following changes are made to the our setup; between the quarter-wave plate ($\frac{\lambda}{4}$(a)) and the photodiode another quarter-wave plate ($\frac{\lambda}{4}$(b)) and polariser are placed. The photodiode was placed after the polariser, as shown in Figure 3.5. The $\frac{\lambda}{4}$(a) is set to one of the maximum optical axis values, while the newly introduced quarter-wave plate $\frac{\lambda}{4}$(b) and polariser are rotated one after the other until a minimum value is reached on photodiode. The second $\frac{\lambda}{4}$ converts the σ^+/σ^- light into linear polarised light, which is orthogonal to the polariser optical axis, so it gets blocked and we get a minimum. If the quarter-waveplate is set to the minimum the second quarter-waveplate will convert σ^+/σ^- light to linear polarised light which is parallel to the polariser's optical axis. We now know how to set σ^+/σ^- and we know the values of the corresponding rotations.

Using Jones matrices for the different optical components in Figure 3.5 the analytical expression for the photodiode intensity is

$$\frac{e^{i\frac{\pi}{2}}}{2\sqrt{2}} \begin{bmatrix} \cos^2\theta & \sin\theta\cos\theta \\ \sin\theta\cos\theta & \sin^2\theta \end{bmatrix} \begin{bmatrix} 1 & 0 \\ 0 & i \end{bmatrix}^2 \begin{bmatrix} 1 & 1 \\ 1 & 1 \end{bmatrix} \begin{bmatrix} \cos 2\theta & \sin 2\theta \\ \sin 2\theta & -\cos 2\theta \end{bmatrix} \times$$

$$\begin{bmatrix} 1 \\ 1 \end{bmatrix} = \frac{e^{i\frac{\pi}{2}}}{2\sqrt{2}} \begin{bmatrix} (\cos^2\theta - \cos\theta\sin\theta)(\sin\theta + \sin 2\theta) \\ (\sin\theta + \sin 2\theta)(\cos\theta\sin\theta - \sin^2\theta) \end{bmatrix} \quad (3.14)$$

In Figure 3.6(a) the analytical expression for the photodiode intensity using Jones matrices is given by

$$\frac{e^{i\frac{\pi}{4}}}{2\sqrt{2}} \begin{bmatrix} \cos^2\theta & \sin\theta\cos\theta \\ \sin\theta\cos\theta & \sin^2\theta \end{bmatrix} \begin{bmatrix} 1 & 0 \\ 0 & i \end{bmatrix} \begin{bmatrix} 1 & 1 \\ 1 & 1 \end{bmatrix} \begin{bmatrix} \cos 2\theta & \sin 2\theta \\ \sin 2\theta & -\cos 2\theta \end{bmatrix} \times$$

$$\begin{bmatrix} 1 \\ 1 \end{bmatrix} = \frac{e^{i\frac{\pi}{4}}}{2\sqrt{2}} \begin{bmatrix} (\cos^2\theta + i\cos\theta\sin\theta)(\sin\theta + \sin 2\theta) \\ (\sin\theta + \sin 2\theta)(\cos\theta + i\sin^2\theta) \end{bmatrix}. \quad (3.15)$$
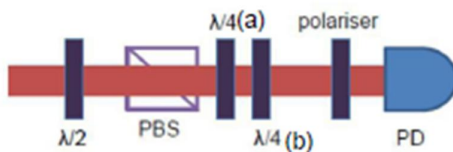
Figure 3.5: Schematic setup showing the conversion of σ^+/σ^- polarised light to linear polarised light.

3.1.6 Implementation

In order to test the quality of σ^+/σ^- we used a setup as shown in Figure 3.6(a). The $\frac{\lambda}{4}$(a) is set to 222^0 ensuring $\sigma^+/\sigma-$ light is created and the polariser and $\frac{\lambda}{4}$(b) are rotated synchronously. Due to the symmetry of $\sigma^+/\sigma-$ the rotation of the polariser should have no effect on the power. We calculated and found the change in power to be 0.4 mW for maximum power of 12 mW. This achieves a polarisability of $\sim 3\%$ which is well within the operational parameters of the MOT. Therefore we now have a method to test the degree of circular polarisability of a beam.

Figure 3.6(b) shows the polarisation detector. The quarter-waveplate (second introduced) and the polariser are coupled together using tubes. The external threads will screw into the tubes of the MOT collimators. The MOT collimators are shown in Figure 3.7. The polarisation detector is held in a stable position while the quarter-waveplate of the MOT collimator is rotated until a maximum or minimum is reached on the photodiode.

Figure 3.6: a) Schematic setup for determining the quality of σ^+/σ^-.b)
Circular polarisation detector.

Figure 3.7: MOT collimators at the University of KwaZulu-Natal (UKZN)
at the Centre of Quantum Technology.

Chapter 4

Magnetic Field Generation

4.1 Helmholtz and Anti-Helmholtz Configuration

To create the Helmholtz configuration two identical coils are axially aligned with the applied current propagating in the same circular direction for both coils. In this way the magnetic field at a particul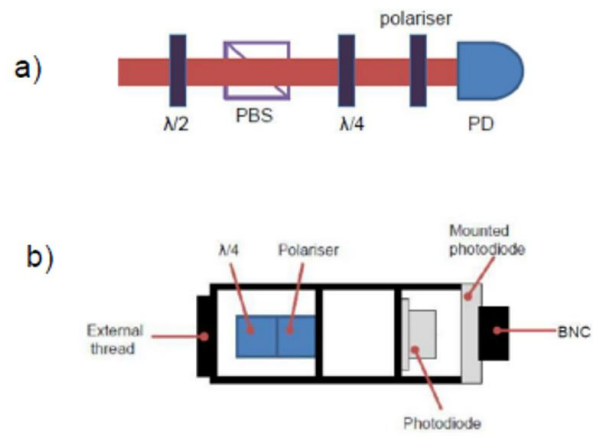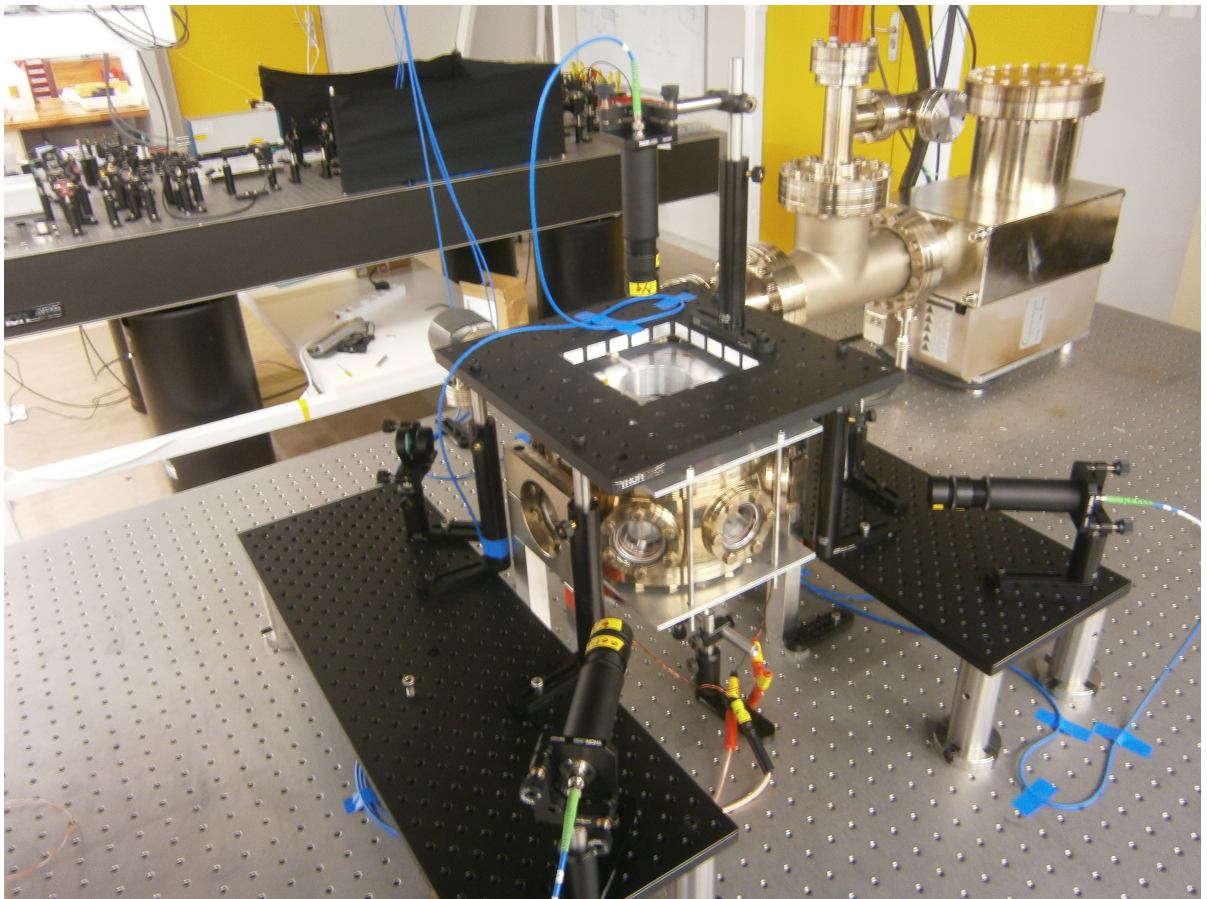ar point is the sum of the contribution of each individual magnetic coil at that point. The magnetic field generated by such coils is easily calculated using the Biot-Savart law. The strength of the magnetic field generated is directly proportional to the number of turns in the coils and the current. It is also proportional to the separation between the coils as well as the radius of the coils. When these coils are at the correct separation they create a homogeneous magnetic field at the central region between the coils. The amplitude of this offset can be controlled by the applied current. To create the Anti-Helmholtz configuration two identical coils are axially aligned with the applied current propagating in the opposite circular direction in each coil. This is possible because the coils now have the currents propagating in opposite direction magnetic field at a particular point is the subtraction of the contribution of each individual magnetic coil at that point. This result creates a sharp magnetic field gradient at the central region with a zero magnetic field at the center in the MOT. The atoms are attracted to this zero magnetic field and are thus trapped. Therefore by controlling the gradient and position of the zero magnetic fields the shape, size and position of the trapped atoms can be easily controlled with the aid of the applied current. [9, 16, 17, 18]

A current passing a single circular loop of wire produces a magnetic field in the central axis of a the loop given by

$$B = \frac{\mu_0 I a^2}{2(a^2 + x^2)^{\frac{3}{2}}},$$ (4.1)

where a is the radius of the loop, x is the axial distance from the centre of

the loop and μ_0 is the magnetic permeability of free space. If we consider two identical coils separated by a distance c, each carrying N turns of wire and with current I flowing in the same direction. The magnetic field along the axis of the coils is given by (Helmholtz configuration)

$$B = \frac{\mu_0 I a^2 N}{2} \left[\frac{1}{(a^2 + (c-x)^2)^{\frac{3}{2}}} + \frac{1}{(a^2 + (c+x)^2)^{\frac{3}{2}}} \right]. \qquad (4.2)$$

The magnetic field gradient and the third derivative at the center of the coil is zero due to coil symmetry and hence the magnetic field is most uniform for the Helmholtz configuration when a is equal to c. With the same identical coils axially separated by a distance c with the current through both coils passing in the opposite sense produces a magnetic field (anti-Helmholtz configuration)

$$B = \frac{\mu_0 I a^2 N}{2} \left[\frac{1}{(a^2 + (c-x)^2)^{\frac{3}{2}}} - \frac{1}{(a^2 + (c+x)^2)^{\frac{3}{2}}} \right]. \qquad (4.3)$$

The magnetic field at the center of the coils is equal to zero due to coil symmetry and the magnetic field gradient is given by

$$\frac{\partial B}{\partial x} = \frac{-3\mu_0 I N a^2 x}{(a^2 + x^2)^{\frac{5}{2}}}. \qquad (4.4)$$

One should take note that the axial gradient is not equal to radial gradient. The gradient along the radial axes is half the value of the axial gradient.

4.2   Optimisation

In the experiment performed in the laboratory the physical parameters of the coils were measured are given in Table 4.1. Each coil was connected to the power supply (PSU) where current and voltage was kept constant at 1 A and 6 V respectively, consuming a power of 6 W. A voltmeter was connected to the SS94A1F Hall PSU current and voltage was kept constant at 0 A and 8 V respectively. The Hall probe SS94A1F is used to determine the magnetic field. This device has very small sensitivity variations and compensates for temperature changes. It has a flux range of ± 100 Gauss. The sensor uses a Hall Effect integrated circuit chip. This provides increased temperature stability and performance. The Laser trimmed thick film resistors and thin film resistors reduce null and gain shifts over temperature. This results in consistent sensitivity from one device to the next. The sensitivity of this device at 25^0C is 25 ± 5 mV/G [19]. Current was applied to the coil and the probe connected to the voltmeter to detect the voltage. A meter ruler was fixed on the table as a guide for the probe to move along the axis through the center of the coil. Raw data of distance of the probe (x-position) and

voltage were recorded and graphical plots of the data were created. The null voltage was also measured, which is the voltage created by stray magnetic fields when the coils are off. This was subtracted from the each magnetic field reading and was than converted to magnetic field units using the probe sensitivity and the magnetic field of the coil was calculated using the value of the probe (25 mV/G) multiplied by the subtraction of the raw data voltage from the null voltage. The expected results of the magnetic field are calculated by Biot-Savart law. The voltmeter was also used to measure the temperature of the coil as current increased.

Table 4.1: Physical parameters of the coils.

Parameters	Value
Inner Diameter of Support	6.5 cm
Wall Thickness of Support	1 cm on base and 0.5 cm on outer surface
Inner Diameter of Coil	8.3 cm
Outer Diameter of the Coil	17.9 cm
Radial Width	4.8 cm
Axial Width	2 cm
Average Diameter	13.5 cm
Number of Loops	656
Length of Wire	270 m
Resistance of Wire	5.9 Ω
Wire Diameter	1 mm
Wire Cross-Sectional Area	0.00785 cm^2
Packing Ratio	0.535

Figure 4.1 represents the schematically diagram of anti-Helmholtz coils which is what was constructed in the lab.

4.2.1 Magnetic Field of a Single Coil

Initially, as a preliminary test on the system, the magnetic field generated was calculated and measured. Figure 4.2 shows the plot for single coil magnetic field plotted against displacement in the axial direction. The blue points correspond to a data set of the experiment and red curve represents theoretical values. It can be immediately seen that the magnetic field decreases exponentially when moving away from its center point. This is expected and it can be seen that there is a high degree of agreement between the experimental and theoretical values.

Figure 4.3 shows a linear dependence between current and magnetic field at a given point. A hall probe was placed at the center of the coils to mea-
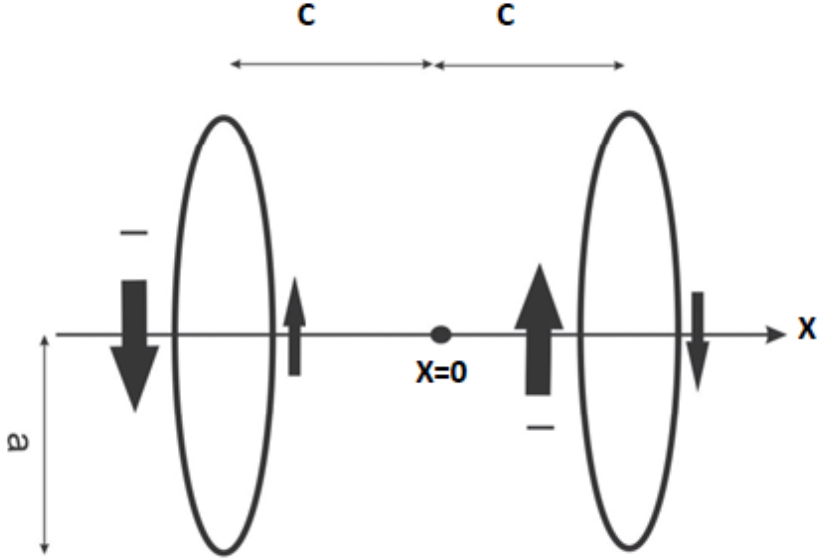
Figure 4.1: Coil axis along which the measurements where taken.

sure magnetic field as a function of current. The blue data points in Figure 4.3 correspond to the theoretical values while the red points are the experimental data. The gradient obtained from the linear plot represents the rate of change magnetic field amplitude per unit change in current. Therefore a slope of 66 G/A means that the magnetic field amplitude will change by 66 Gauss for every 1 A applied to the coils. Both of these outcomes have a very high degree of agreement with the theoretical results.

4.2.2 Thermal Properties

It is important to know the thermal properties of the coils as the electrical properties change with temperature. In addition, if the coils get too hot they heat-up the vacuum chamber and thus increase the rate of outgassing in the chamber. This increases the base pressure and thus decreases the lifetime of the atom cloud. A thermocouple was attached to a coil to measure the temperature as a function of power/current. The temperature against power graph was observed to give the plot in Figure 4.4. The figure gives a linear relationship which has a gradient of 0.83 ^{0}C/W, this effect simply means when more power is added on the coil(s) in terms of increasing current temperature also increases. Thus the expected temperature of the coils can be given by

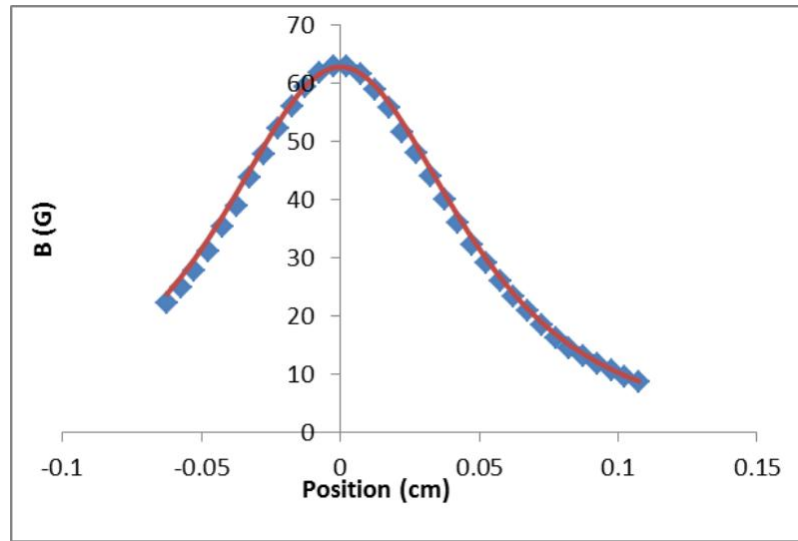$$T = 0.84P_{coil} + T_{room}, \tag{4.5}$$

Figure 4.2: Magnetic field generated by a single coil. The red line represents theoretical values and the blue dots represent experimental values.

where T_{room} is the room temperature, P_{coil} is the power in the coil. From the plot , a power of greater than 64 W or 2.86 A should not be applied to these coils to prevented overheating and adverse effects on the vacuum system.

4.2.3 Helmholtz Coils Test

The magnetic field in the axial direction was measured for 3 different coil separations 0.025 m (Separation < radius of the coils), 0.0655 m (separation = radius of the coils), and 0.088 m (separation > radius of the coils) while current in the coils was kept constant. The magnetic field for each separation was plotted against the probe displacement and Figures 4.5, 4.6 and 4.7 were obtained for Helmholtz coils. In each plot the red line represents the theoretical data while the blue data points are the experimental readings. The green and purple lines represent theoretical curves for coil 1 and coil 2 respectively. The shape of the Helmholtz configuration is obtained for the three seperations. There is some asymmetry in the coils, this can be seen as the difference between the experimental and theoretical values are different for both sides. this is probably due to the fact that both coils are not wound identically. The error in the readings, according to the Gauss/Teslameter manual, is 0.25% of the measured value. It appears that one coil is slightly stronger then the other coil. These were the limiting factors in determining the characteristics of the constructed coils.
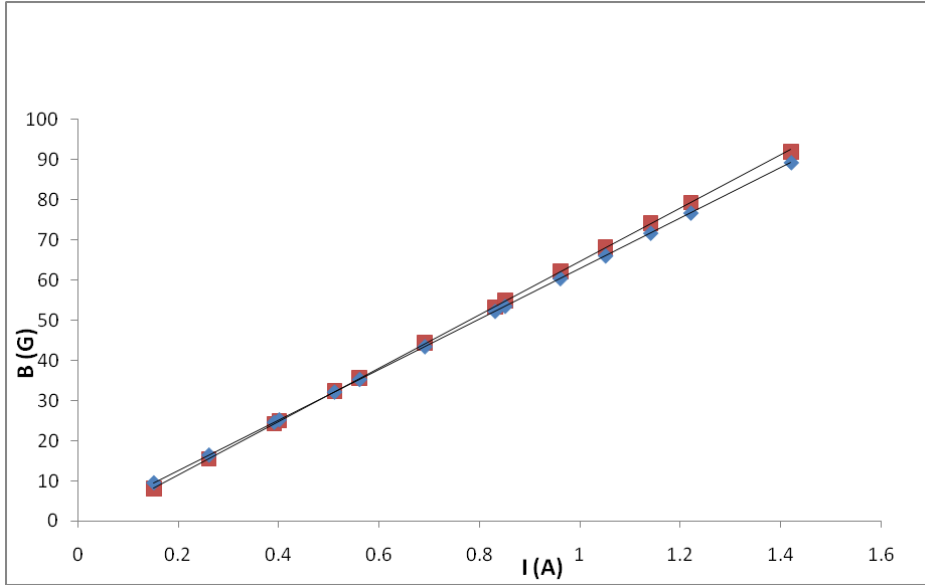
26

Figure 4.3: A plot showing magnetic field (**B**) against current (**I**) for a single coil at a particular point. The two lines are lines of best fits for the blue and red points.

4.3   3-D MOT Calculation Measurement

One particular magnetic field shape is required for our experiment. We need the field to have a high gradient at the center of the trap. This is achieved by a set of anti-Helmholtz coils. The magnetic field in the axial direction was measured for 3 different coil separations 0.025 m (separation< radius of the coils), 0.0655 m (separation = radius of the coils), and 0.088 m (separation>radius of the coils) while current of the coils was kept constant. The magnetic field for each separation was plotted against the probe displacement and Figures 4.8, 4.9 and 4.10 were obtained for anti-Helmholtz coils.The shape of the Anti-Helmholtz was successfully obtained for all the three separations (less than the radius, equal to the radius, and greater than the radius). All of these outcomes have a very high degree of agreement with the theoretical results. The theoretical plots have a R-squared value of 0.098 for 0.026 m separation, R-squared value of 1 for 0.0655 m separation and R-squared value of 0.998 for 0.08 m separation. The experimental plots have a R-squared value of 0.995 for 0.026 m separation, R-squared value of 0.995 for 0.0655 m separation and R-squared value of 0.998 for 0.08 m separation. In each plot the red line represents the theoretical data while the blue data points are for experimental readings.

The values of the slopes for these three separations were calculated by se-
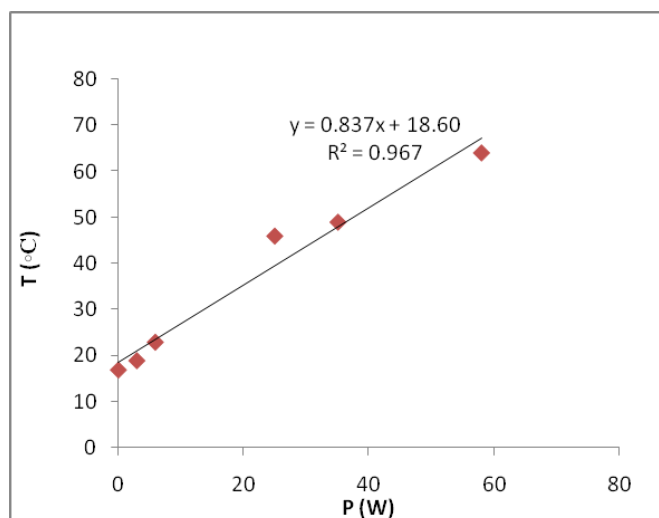
Figure 4.4: Temperature (**T**) of coil as the power (**P**) is increased.

lecting few data points in each plot of Figures 4.8, 4.9, and 4.10 that have a linear relationship in the whole plot. These data points were plotted individually in Figures 4.11, 4.12 and 4.13. The blue line represents the data points for the theoretical values and the dotted red points are experimental values. Table 4.2 shows the gradients achieved in the different separations. The measurements made for these coil arrangements agree with calculations and they are adequate for this experiment. As the separation between the two coils is increased the gradient decreases. The gradient is dependent on the separation and amplitude of the peaks. The highest axial gradient is 16.21 G/m and the highest radial gradient for both axes is 8.11 G/cm. The experimental results obtained in the laboratory were compared with the theoretical plot and human errors and systematic errors was taken into consideration. These comparisons were quite reasonable.

Table 4.2: Anti-Helmholtz coils magnetic gradient at different separations.

Separation	Axial Gradient	Radial Gradient (for both axes)
0.026 m	16.21 G/cm	8.11 G/cm
0.0655 m	9.98 G/cm	4.99 G/cm
0.08 m	6.91 G/cm	3.46 G/cm
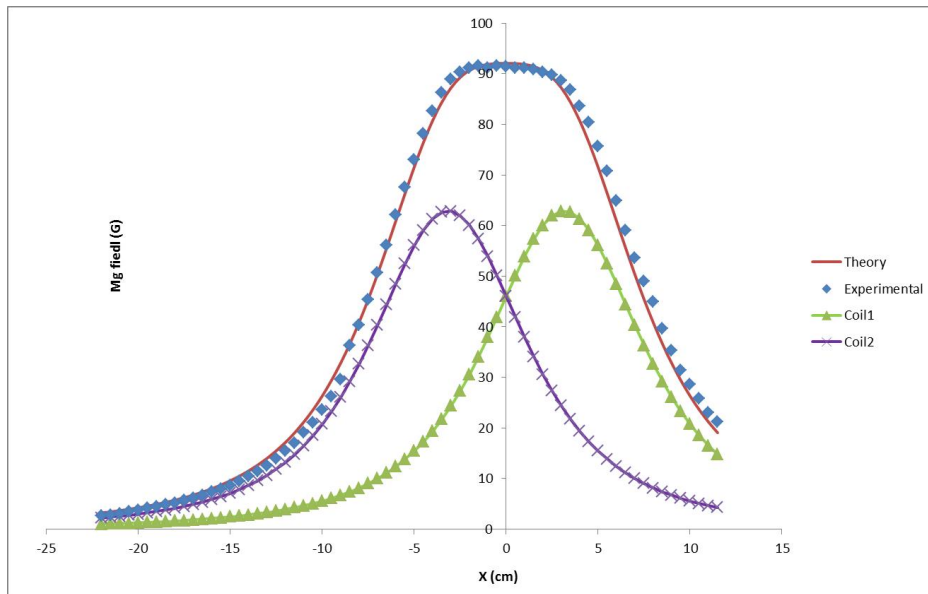
Figure 4.5: The plot of magnetic field (**B**) against position (**x**) when the separation is less than the radius of the coils.
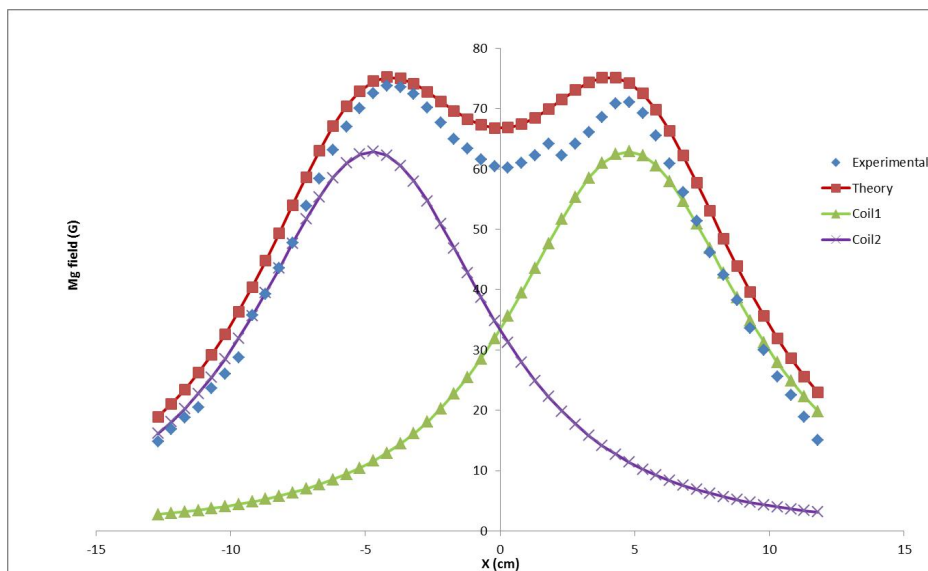
Figure 4.6: The plot of magnetic field (**B**) against position (**x**) when the separation is equal to the radius of the coils.
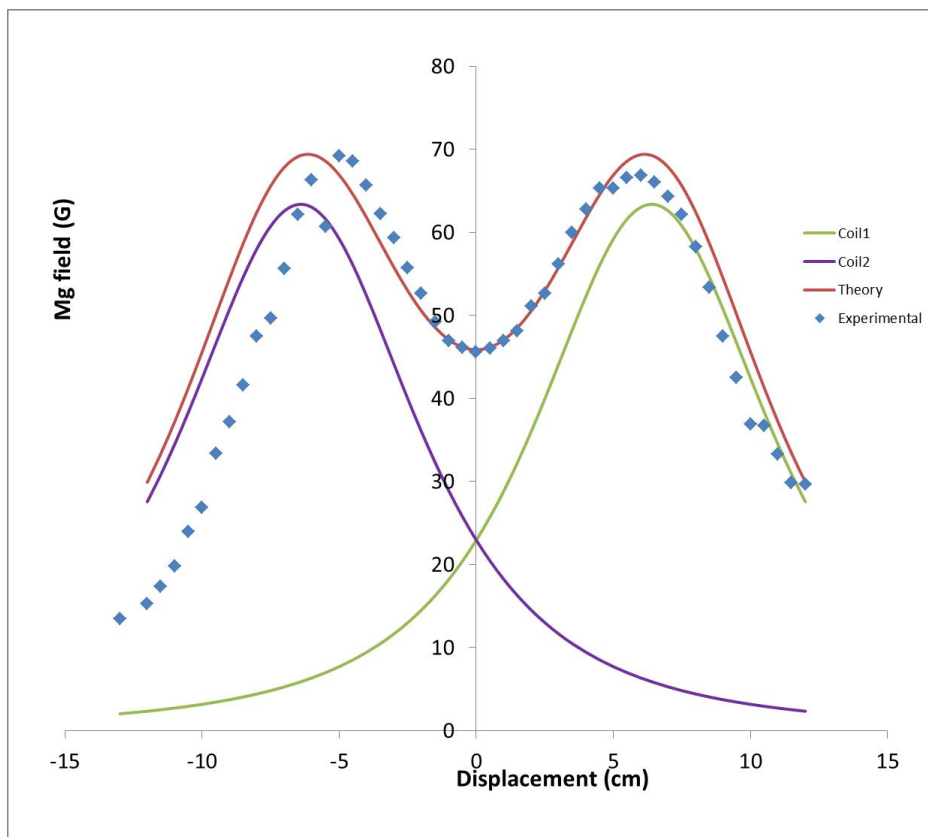
Figure 4.7: The plot of magnetic field (**B**) against position (**x**) when the separation is more than the radius of the coils.
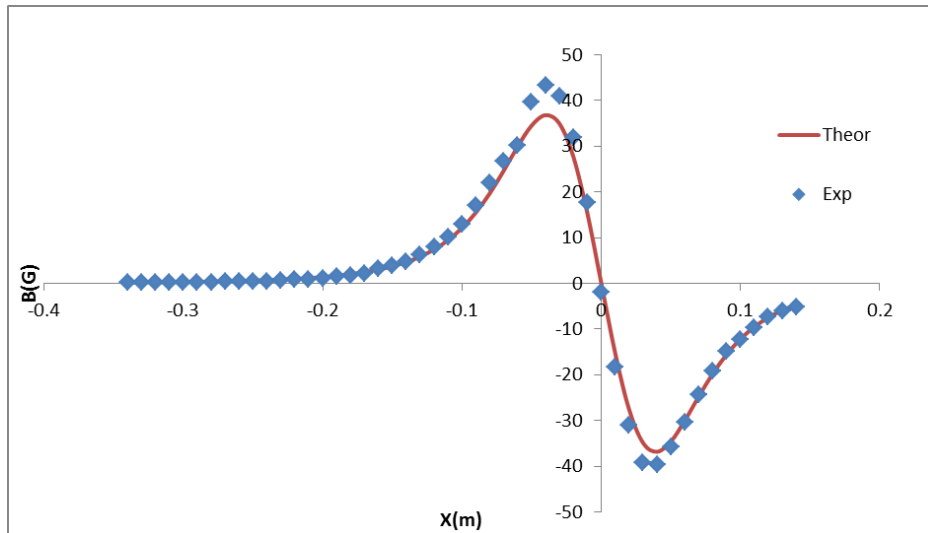
Figure 4.8: This plot shows magnetic field (**B**) against position (**x**) for anti-Helmholtz coils when the separation is less than the radius of the coils.
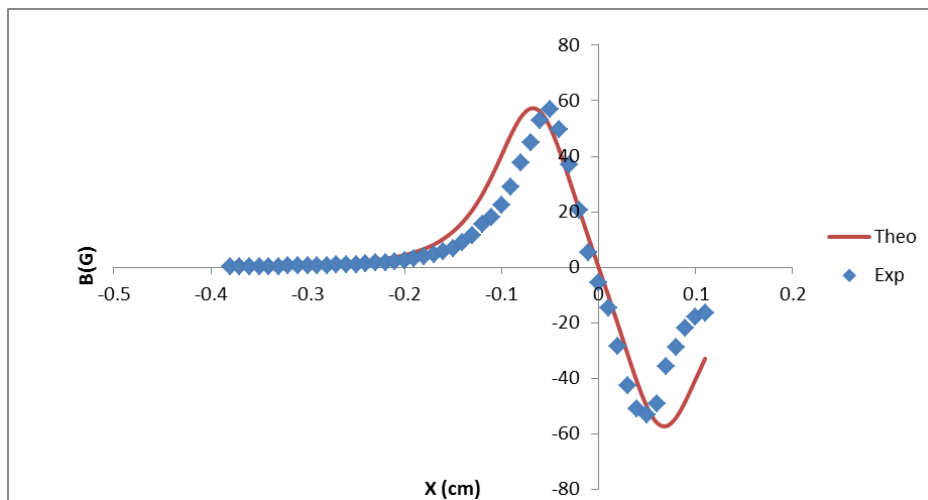
Figure 4.9: A plot showing magnetic field (**B**) against position (**x**) for anti-Helmholtz coils when the separation is equal to the radius of the coils.
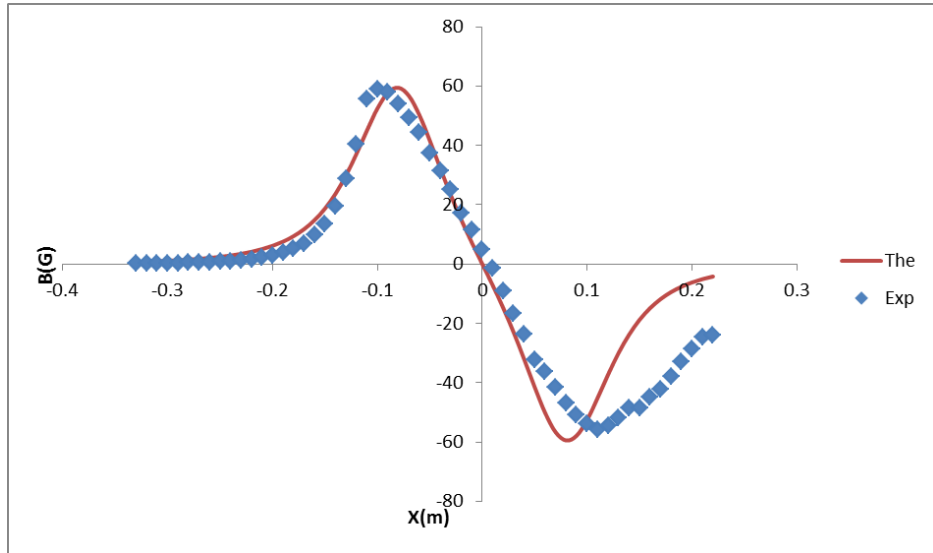
Figure 4.10: A plot showing magnetic field (**B**) against position (**x**) for anti-Helmholtz coils when the separation is greater than the radius of the coils.
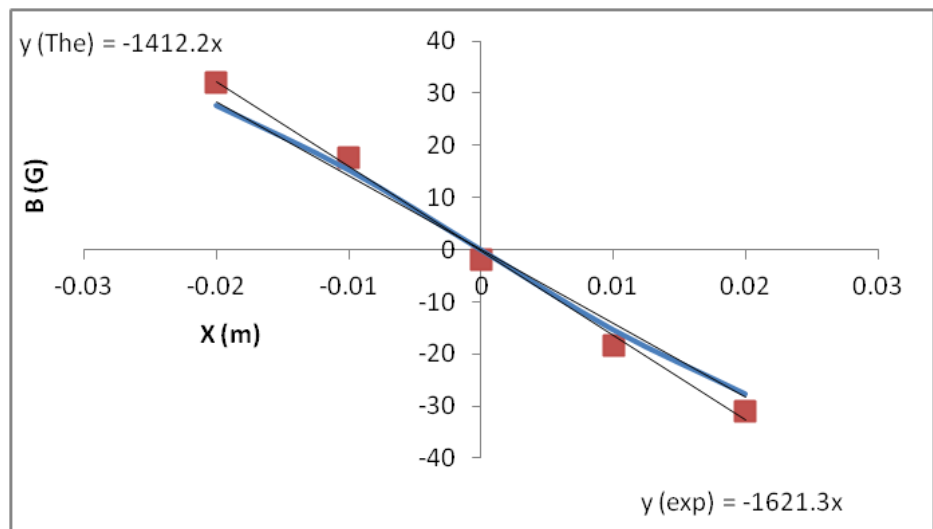
Figure 4.11: Magnetic gradient when the separation is less than the radius of the coils. The black lines represent lines of best fit required to calculate gradient.
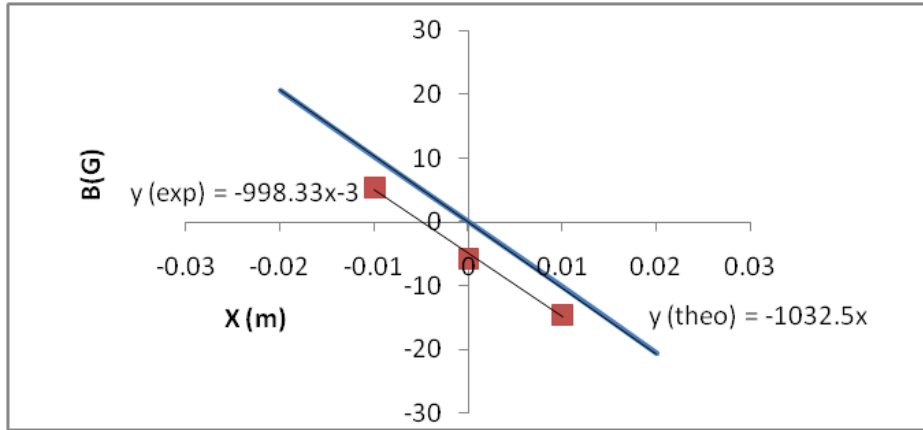
Figure 4.12: Magnetic gradient when the separation is equal to the radius of the coils. The black lines represent lines of best fit required to calculate gradient.
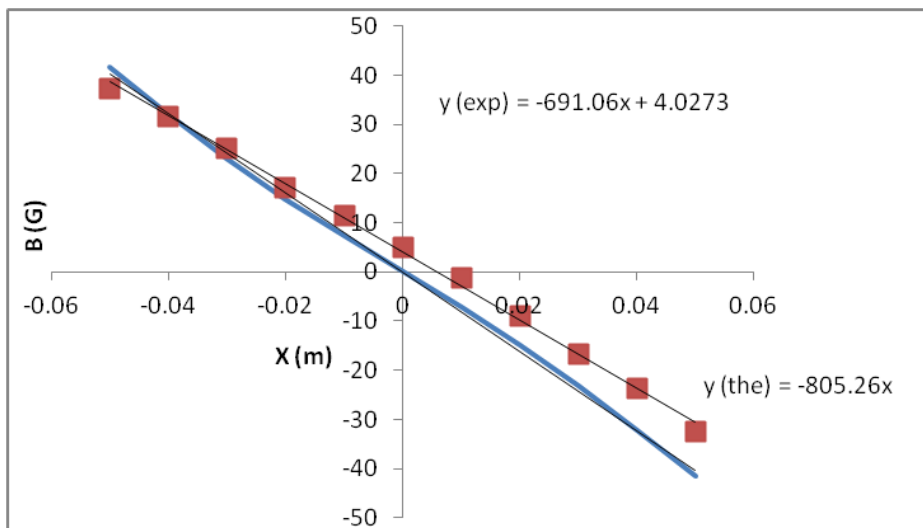
Figure 4.13: Magnetic gradient when the separation is greater than the radius of the coils. The black lines represent lines of best fit required to calculate gradient.

Chapter 5

Fluorescence Detection System

5.1 Number of Atoms

When all the vacuum, optical and electrical components of the MOT are put together in a correct manner, it is possible to create a cloud of cold atoms. The advantage with the MOT setup is its insensitivity to minor inaccuracies which may be present in the beam alignment, overlap of the magnetic zero with the exact intersection of the beams, beam polarization and detuning. The MOT can be optimised once some atoms are trapped. The optimisation requires the alignment of the beams to the exact centre of the magnetic field. Another variable used in this optimisation is the power supplied to each of the MOT beams, ideally keeping all beams equal. The background vapour in the chamber is high enough to see fluorescence from the orthogonal cooling beams. When the cloud has been optimised it is possible to look at the MOT characteristics.

5.1.1 Theory

For optimisation of the experimental setup it is crucial to have a method to determine the number of atoms that have been trapped. This can be measured by monitoring the scattered fluorescence from the MOT with the aid of a photodiode. The total power that is measured in the photodiode is give by [20]

$$P = \epsilon_{ph} \frac{\Omega_{image}}{4\pi} N_A R_{scat}, \tag{5.1}$$

where ϵ_{ph} is the energy of the photon, Ω_{image} is the solid angle subtended by the collection lens of the imaging system, N_A is the number of atoms and R_{scat} is the scattering rate. The solid angle is given by

$$\Omega_{image} = \frac{\pi d_{image}}{D_{lens}^2}, \tag{5.2}$$

where D_{lens} is the diameter of the first lens and d_{image} is the distance between the centre of MOT and the first lens. By manipulating equation 5.1, we see that the number of atoms can be calculated by the following equation

$$N_A = \frac{P}{R_{scat}} \frac{4\pi}{\Omega_{image}}.$$ (5.3)

By using a large area lens close to the MOT and focussing the collected light on the photodiode the percentage of scattering light collected will be increased.

5.1.2 Optical Setup

An imaging system that has two lenses is used to focus light from the cold cloud onto the photodiode. The lenses and are placed within a tube system to prevent any ambient light from entering the setup and to allow the adjustment of distances between lenses and photodiode sensor. A schematic of the setup is shown in Figure 5.1. As predicted by equation 5.3 the amplitude of light falling on the PD is directly proportional to the number of trapped atoms. The output of the photodiode is sent to an electronic voltage and to the PC for analysis.
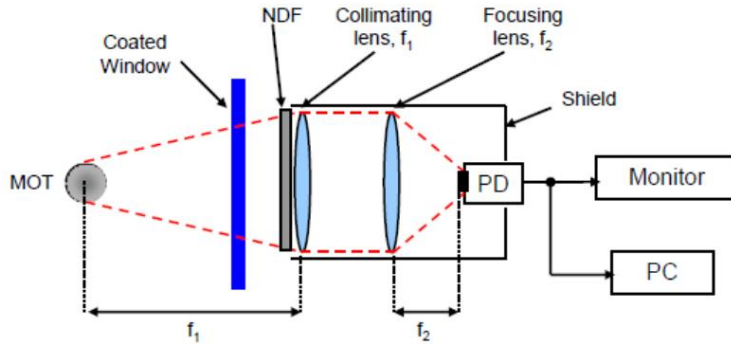
Figure 5.1: Number of Atoms optical setup.

5.1.3 Electronics

The signal from the fluorescence photodiode is sent to an electronic circuit, as shown in Figure 5.2. When the light falls on the photodiode, a current is created. This current is then fed through a 1 MΩ resistor as part of a current to voltage (I-V) converter. This voltage is then sent to an amplifier with a variable gain which is given by R_2/R_1. As it is shown in Figure 5.2

these resistors are variable, and thus allow a variety of gain dependent on the amount of light on the photodiode. The three switches allow for nine levels of gain. Which are shown in Table 5.1. This circuit allows us to monitor the photodiode signal on an oscilloscope and voltmeter. This circuit was designed by me and built by Mr Enoch Chekure, the Senior Lab Technician in the School of Chemistry and Physics.
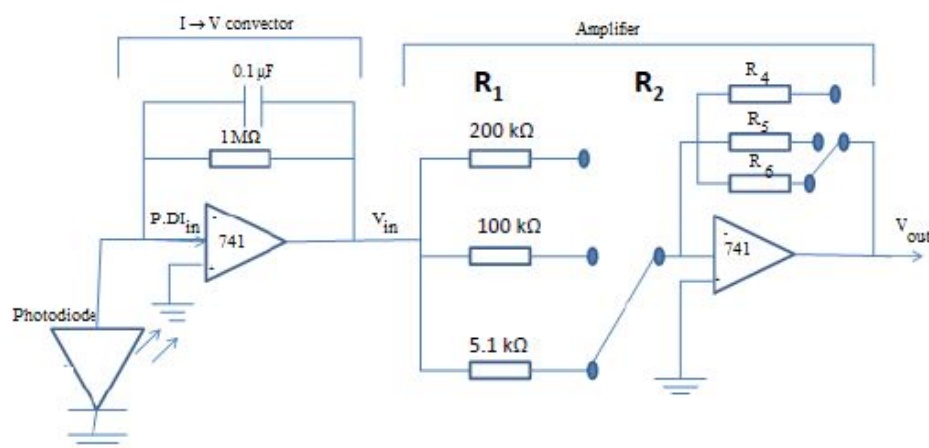
Figure 5.2: Photodiode circuit used to collect scattered fluorescence. The signal from the fluorescence photodiode is sent through this circuit before being recorded on an oscilloscope and a digital voltmeter. Here R_4, R_5 and R_6 is equal to 100 kΩ, 510 kΩ and 1 MΩ respectively.

Table 5.1: Gain settings for current and voltage converter

Resitor1	Resistor2	Gain
200 kΩ	100 kΩ	0.5
100 kΩ	100 kΩ	1
200 kΩ	510 kΩ	2.55
100 kΩ	510 kΩ	5.1
5.1 kΩ	100 kΩ	19.6
5.1 kΩ	510 kΩ	100
200 kΩ	1 MΩ	5
100 kΩ	1 MΩ	10
5.1 kΩ	1 MΩ	196

5.2 MOT Size

5.2.1 Theory

The density distribution of the MOT is Gaussian and is given by

$$G(x) = a_G \exp[-(\frac{x - b_G}{2\sigma_{stdv}^2})^2], \tag{5.4}$$

where b_G is the mean position, σ_{stdv} is the standard deviation and a_G is the peak amplitude. The peak amplitude is given by

$$a_G = \frac{1}{\sigma_{stdv}\sqrt{2\pi}}. \tag{5.5}$$

The diameter of the cloud can be defined as the full-width at half maximum (FWHM) and also as the $\frac{1}{e}$ value. The MOT is loaded when the magnetic field is switched on and atoms from the background vapour are cooled and trapped at that time. The rate of capture of atoms from the background vapour is given by [12, 9, 16]

$$R_{capt} = \frac{\rho_{bg} V_{trap}^{\frac{2}{3}} \nu_{capt}}{2} (\frac{m_A}{2k_B T_{bg}})^{\frac{3}{2}}, \tag{5.6}$$

where ρ_{bg} is the density of the background vapour, V_{trap} is the trapping volume, ν_{capt} is the capture velocity below which atoms will be trapped and T_{bg} is the temperature of the background vapour. The capture velocity is given by [12, 9, 16]

$$\nu_{capt} = \sqrt{\frac{\hbar k_0 \Gamma_A L_{OM}}{2m_A}}, \tag{5.7}$$

where L_{OM} is the optical molasses capture dimension. When the atom cloud begins to form there are loss mechanisms which cause atoms to be lost from the trap. These mechanisms are collisions between the trapped atoms and the background vapour, and collisions between the trapped atoms in the MOT. The MOT now enters a steady state where the capture rate and loss rate are in equilibrium, this results in a steady state number of atoms, N_S trapped in the MOT.

The lifetime of the MOT, is described as the time it takes for the number of atoms to reduce to $\frac{1}{e}$ of the steady state number of atoms, with the cooling beams and magnetic field still in place to continue trapping atoms from the background vapour.The Rb dispensers are switched off, the density of the background Rb vapour and the capture rate reduce to zero. The population of the MOT then decreases due to collisions between trapped atoms and the non-rubidium background vapour. The trap lifetime, τ_{life}, can be measured by monitoring the fluorescence decay on a photodiode. This is a measure of the trapped atom interaction with non-Rb background atoms. The lifetime is independent of the number of trapped atoms.

5.2.2 Imaging

An imaging system that has two lenses is used to focus the light from the cloud on to the CCD sensor. The lenses are enclosed within a tube system to reduce any ambient light and to allow for distances between lenses and the CCD sensor to be adjusted. A schematic of the imaging system is shown in Figure 5.3. The output from the CCD sensor is sent to two locations, it is sent to a monitor for real-time viewing of the cloud and to the video card of a computer where it is recorded.
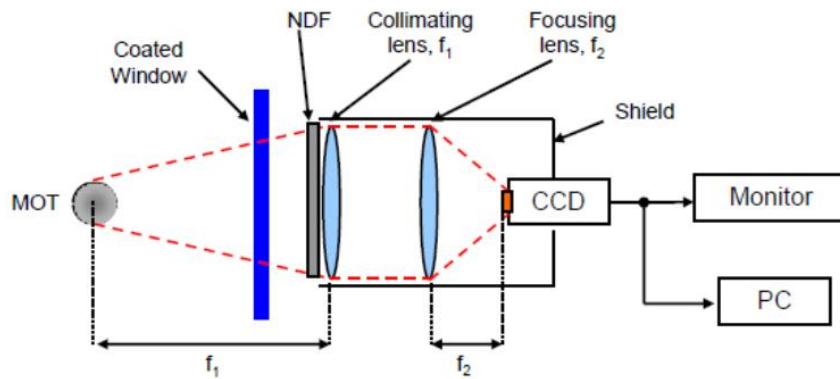

Figure 5.3: The imaging system.

5.3 Automation of Cloud Analysis

LabVIEW was used to create the automation programme. The programme was written by me and Micheal Morrissey. LabVIEW is a graphical programming language developed for interfacing a PC and PCI cards with external hardware. Its interface is based around a user created front panel which is designed to mimic the front panel of a physical control box, with switches, toggles and dials, and a back panel which uses self-contained virtual instruments (VIs) and wires to manipulate and direct data. LabVIEW is not very different from any other computer language, but its modular format and its powerful interface with hardware means that it is very adaptable to different problems. A National Instruments (NI) card is used to interface with the experiment. The card that is used to output all signals to the experiment is, the NI PCIe-6320. This card provides 16 analog Input channels and 24 digital output and input channels.

5.3.1 Number of Atoms

Figure 5.4 shows the automation program. The programme uses equation 5.3 to determine the number of atoms from the photodiode signal. It must therefore take into account the experimental parameters of both the setup and the imaging system. The program is broken into several sections which can be described as follows:

The Voltage chart shows the raw data from the photodiode, while in the Imaging panel its where the user defines the imaging parameter of the experimental setup. These input parameter are used to determine the solid angle subtended by the imaging system, as well as the sensitivity of the imaging system. In the MOT parameter panel the user inputs the parameter of the MOT configuration such as the total power of the MOT beams and their detuning from the atomic cooling transition. The Save to file panel allows the user to define the file to which it is saving the data as well as when to begin and stop saving data. In the saved file all input parameters are saved as well as the raw data and the calculated number of atoms. The Background compensation panel allows the user to compensate for background fluorescence. The 'set' button in pressed when the MOT is off and the background fluorescence level is subtracted from the raw data before the number of atoms is calculated.The Number of atoms chart displays the number of atoms determined from the raw data based on the user defined input parameters. The number of atoms is calculated from Equation 5.3. If the background compensation is enabled, the effect of background fluorescence has been compensated for in the data shown.

5.3.2 Size of MOT

When the MOT image has been captured and sent to the PC, it is then sent to the LabVIEW programme. Figure 5.5 shows the LabVIEW programme. The results of the program were simulated using an image of atoms that were trapped at UKZN in 2009. The program is broken into the following sections:

The Raw Image chart shows the captured image of the MOT. The region of interest (ROI) is selected from the raw image. The Region of Interest chart shows a selected region from the raw image. The Intensity plot of ROI chart graphs the intensity of ROI. The Pixel calibration panel shows by how much the captured image needs to calibrated.The Result summary panel shows the characteristics of the MOT.
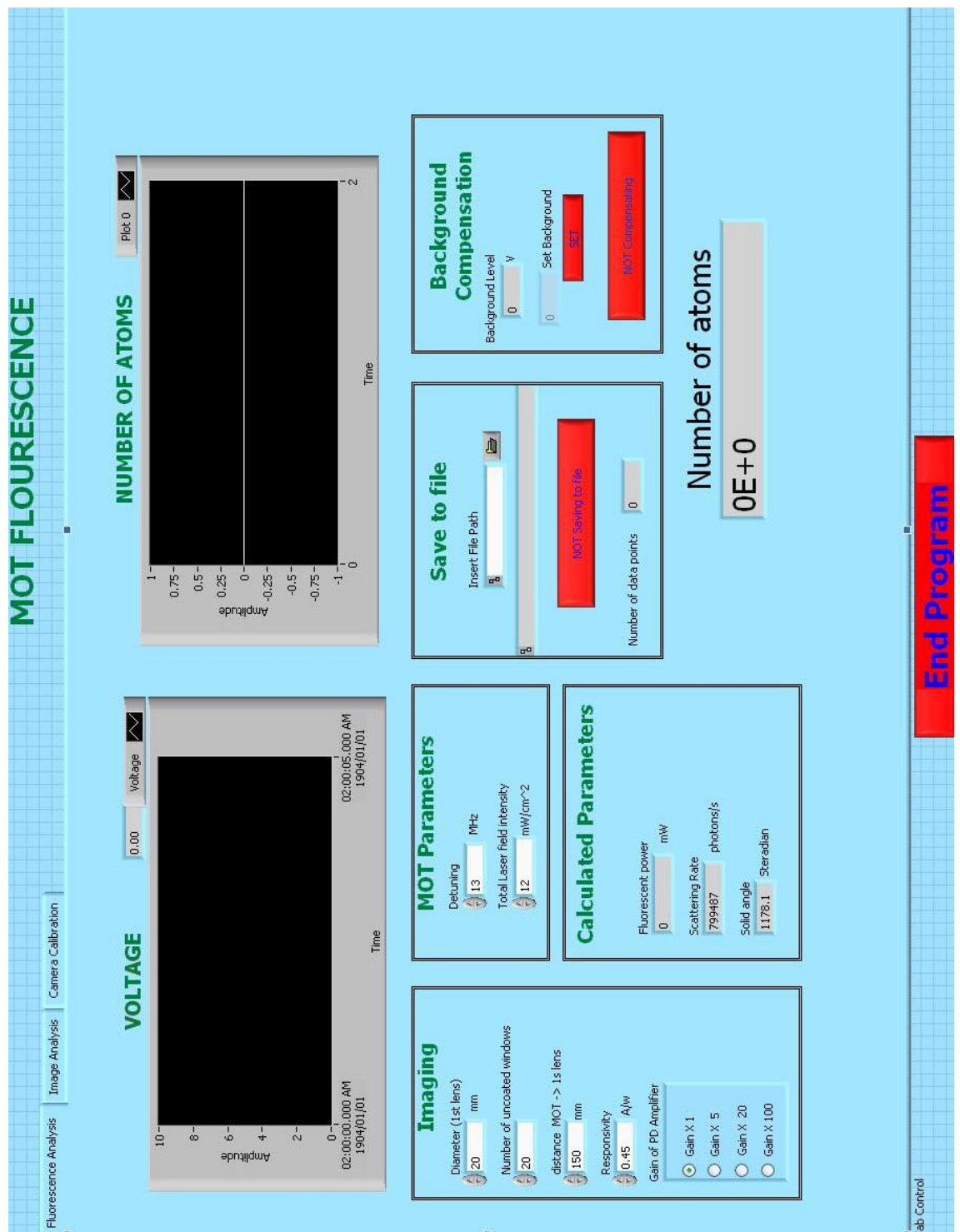
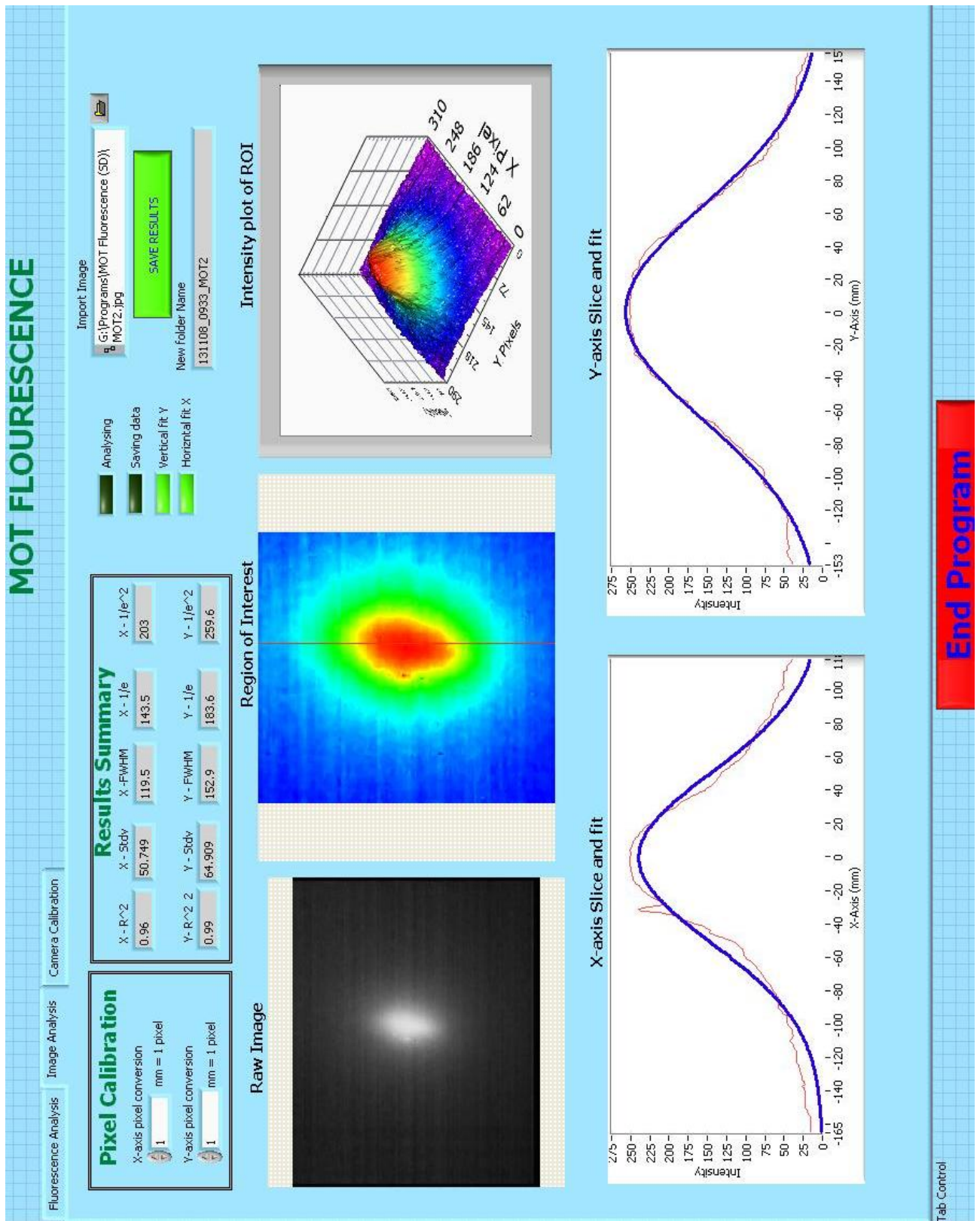Figure 5.4: LabVIEW programme to monitor fluorescence from the MOT.

Figure 5.5: Analysis of fluorescence image from trapped atoms in LabView.

Chapter 6

Discussion and Conclusion

This work that is presented in this dissertation has investigated the devices that are needed when constructing a cold atom experiment. Basic theory of laser cooling has been discussed and explained in order to have a clear understanding of what it entails. The cold atoms are produced using a standard six-beam MOT, which relies on polarisation gradient cooling and magnetic trapping techniques. A device which analyses if we have circular polarised beams was designed and constructed. A pair of anti-helmholtz coils were also designed to provide a linear gradient magnetic field in the trapping cell to add Zeeman splitting for sub-Doppler cooling. The coils were constructed to the specific requirement for our experiment magnetic coils. When the MOT is setup, technical methods are required to measure and characterise many parameters of the cold atom cloud. A LabVIEW program was therefore designed to study the MOT characteristics.

In the laboratory we have successfully constructed a system for laser cooling and trapping of atoms. Experience with the various equipment in the laboratory has been obtained. Devices needed for the construction of the MOT have been designed and constructed. A program to monitor the MOT characteristics is now operational. The trapping of atoms has not yet been realised. This is why we do not have characteristics for the MOT.

The overall goal of the experiment is to achieve a Bose-Einstein condensation (BEC). This will involved further experimental steps such as optical pumping, magnetic trapping and evaporative cooling. This will result in an ultra-cold experimental facility that will allow researchers to investigate the quantum collective effects of atoms at UKZN.

Bibliography

[1] H.J. Metcalf and P. Van der Straten, *Laser Cooling and Trapping*, Springer-Verlang 1999

[2] C.J. Foot, *Atomic Physics*, Oxford, 2005

[3] W. D. Phillips, Laser cooling and trapping of neutral atoms, Reviews of Modern Physics, Vol. 70, No. 3, July 1998

[4] M. Stephens and C. E. Wieman, High collection efficiency in a laser trap, Phys. Rev. Lett. 72, 3787, 1994

[5] M.J. Morrissey Manipulation tools for laser- cooled rubidium atoms: ultrathin optical fibres and magnetic diffraction gratings, PhD thesis,Cork Intistute of Technology, 2009

[6] A. K. Mohapatra and C. S. Unnikrishnan, High sensitivity probeabsorption technique for time-of-flight measurements on cold atoms, Pramana J. Phys. 66, 1027, 2006

[7] R.R. Silva, K.M.F. Magalhes, E.A.L. Henn, L.G. Marcassa, V.S. Bagnato,Temperature determination for magneto optical trapped atoms using a single parameter transient absorption Optics coms. 265, 526-531, 2006.

[8] J. Lawall, S. Kulin, B. Saubamea, N. Bigelow, M. Leduc and C. Cohen-Tannoudji, Three-dimensional laser cooling of helium beyond the single-photon recoil limit, Phys. Rev. Lett. 75, 4194, 1995

[9] P.F. Griffin, Laser Cooling and Loading of Rb into A Large Period, Quasi-Electrostatic, Optical Lattice, PhD thesis, Durham University, 2005

[10] P. D. Lett, R. N. Watts, C. I. Westbrook, W. D. Phillips, P. L. Gould and H.J. Metcalf, Observation of atoms laser cooled below the Doppler limit, Phys. Rev. Lett. 61, 169, 1988

[11] Daniel A. Steck, Rubidium 87 D Line Data, available online at http://Steck.us/alkalidata (revision 2.1.2, 12 August 2009)

[12] U. D. Rapol, A. Wasan and V. Natarajan, Loading of a Rb magneto-optic trap from a getter source, Phys. Rev. A 64, 0234u 02, 2001

[13] G.L. Weissler and R.W. Carlson, editors. Methods of Experimental Physics:Vacuum Physics and Technology. Academic Press, 1979.

[14] M. H. Anderson, J. R. Ensher, M. R. Matthews, C. E. Wieman and E. A.Cornell, Observation of Bose-Einstein condensation in a dilute atomicvapor, Science 269, 198, 1995

[15] F.L Pedrotti and L.S Pedrotti,Introduction to Optics, 2nd edition, Prentice-Hall International, inc, (1993), ISBN 0-13-016973-0

[16] P. Tierney, Magnetic Trapping of an Ultracold ^{87}Rb-^{133}Cs Atomic Mixture, PhD thesis, Durham university, 2009

[17] M.L. Harris, Realisation of a Cold Mixture of Rubidium and Caesium, PhD thesis, 2008

[18] David J. DeTroye and Ronald J. Chase, the Calculation and Measurement of the Helmholtz Coils Field, ADA286081, page. 5-9, 1994.

[19] http://za.rs-online.com/web/

[20] M. D. Barrett, J. A. Sauer, and M. S. Chapman, All-optical formation of an atomic Bose-Einstein condensate, Phys. Rev. Lett. 87, 010404, 2001